

A coupled scaled boundary finite element and phase-field algorithm for seismic loading

Yue Zhuo^{a,b}, Degao Zou^{a,b,*}, Kai Chen^{a,b,*}, Jingmao Liu^{a,b}, Yongqian Qu^{a,b}, Guoyang Yi^{a,b}

^a The State Key Laboratory of Coastal and Offshore Engineering, Dalian University of Technology, Dalian, Liaoning 116024, China

^b School of Infrastructure Engineering, Dalian University of Technology, Dalian, Liaoning 116024, China

ARTICLE INFO

Keywords:

SBFEM
Concrete gravity dam
Reciprocating seismic load
Earthquake damage

ABSTRACT

Seismic-induced damage, integral to the safety evaluations of major engineering projects, persists as a key focus of research worldwide. Based on the Scaled Boundary Finite Element Method (SBFEM) and the Phase-Field Method (PFM), a coupled algorithm tailored for reciprocal loading was introduced in this paper, integrating strategies including "closure constraints," "numerical threshold strategy," and "subdomain block integration." Adopting object-oriented principles, a universal coupling solution framework has been built and seamlessly embedded within GEODYNA, a self-developed finite element software system. The accuracy was validated through rigorous benchmark tests. The entire process of crack initiation, propagation, and dynamic opening-closing cycles in the Koyna concrete gravity dam was reproduced. Furthermore, the effect of mesh size and computational timestep on the structural seismic response, crack localization, and the extent of damage in the dam were explored. The outcomes demonstrated that the SBFEM-PFM coupling algorithm performs effectively and meets the engineering precision criteria for seismic evaluations and reinforcement analyses of crucial structures.

1. Introduction

Analytical techniques for assessing structural damage and fracture play a crucial role in capturing the intricate mechanical behaviors, failure patterns, and vulnerable zones within major engineering under seismic loading. These methods are vital for improving aseismic design and reinforcement strategies, contributing significantly to earthquake resilience and safety in modern engineering practice.

Currently, the primary methods for analyzing seismic-induced damage and fracture in structures include the Plasticity Damage Model (PDM), the Cohesive Zone Model (CZM), the eXtended Finite Element Method (XFEM), etc. Representative researches are as follows: The PDM, expanded by Lee et al. [1], has been applied to concrete structures under cyclic loading and further adapted to steel frameworks [2], nuclear facilities [3,4], underground walls [5], and concrete-faced rockfill dams [6-8]. The CZM, building on foundational work by Barenblatt [9] and Dugdale [10], has been refined for nonlinear fracture analyses in concrete by Jirásek et al. [11], with subsequent adaptations across various structures [12-18]. The XFEM, initially proposed by

Belytschko et al. [19], has undergone extensive developments and enhancements [20-22], enabling sophisticated analyses of structural damage under earthquakes [23-29]. Additionally, the Phase-Field Model (PFM) [30-33], based on the F-M variational principle [19,34], has transformed fracture analysis by eliminating predefined fracture criteria, integrating seamlessly with existing finite element models, and facilitating multifield analyses [35], albeit at a high computational cost [36-40]. Currently, most studies have focused on small-scale components with an emphasis on mechanism analysis. Applications to large-scale engineering structures have been mostly limited to static fracture analysis [41-44].

Cross-scale meshing has emerged as a strategic approach to reduce computational magnitude while maintaining both accuracy and efficiency. Several techniques have been developed for its implementation, including the Multi-Point Constraint Method, the Finite Element Mesh-Free Coupling Method, the Polygonal Finite Element Method, and the SBFEM. Notably, the SBFEM, proposed by Song and Wolf [45-50], is a semi-analytical approach known for its high precision and flexibility in modeling complex elements, earning widespread endorsement and

* Corresponding authors.

E-mail addresses: zoudegao@dlut.edu.cn (D. Zou), chenkai@dlut.edu.cn (K. Chen).

<https://doi.org/10.1016/j.enganabound.2024.106009>

Received 1 July 2024; Received in revised form 18 October 2024; Accepted 18 October 2024

Available online 24 October 2024

0955-7997/© 2024 Elsevier Ltd. All rights are reserved, including those for text and data mining, AI training, and similar technologies.

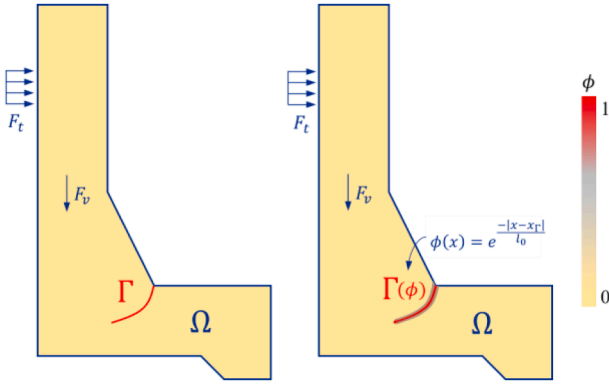


Fig. 1. Phase-field approximation.

promotion within the engineering community. For instance, to enhance the computational efficiency of dynamic analysis for subway tunnels, Chen et al. [51] used a combination of SBFEM-FEM, Octree, and element similarity technology. Zhao et al. [52] and Zhang et al. [53–55] should be commended for utilizing the SBFEM to flexibly calculate the complex soil mechanics problems, driving the research on soil-structure interaction. To examine the interaction between a plate and a multi-layered elastic foundation, Ye et al. [56] employed the SBFEM-FEM coupling techniques. Jiang et al. [57] innovatively developed machine learning algorithms integrated with SBFEM, facilitating the implementation of effective preventive maintenance strategies. In addition, relevant researchers [58–61] analyzed other types of engineering structures using the SBFEM-FEM coupling method. Particularly, pioneering studies [36, 62–68] have innovatively developed the SBFEM-PFM approach by integrating SBFEM and PFM, etc. This advanced method is applied for precise crack analysis using small-scale components in diverse scientific fields.

Nevertheless, the prevailing SBFEM-PFM coupling methods still face challenges in the opening-closing of cracks under seismic loads. The commonly used mesh size standards and element integration techniques impose significant computational burdens, struggling to seismic response analysis of large-scale structures. In light of this, the "closed constraint," "numerical threshold strategy," and "subdomain block Hammer integration" are introduced within the SBFEM-PFM model in this paper. Adhering to object-oriented principles and utilizing the self-developed software GEODYNA, the SBFEM-PFM coupling solution framework was constructed and integrated. The computational accuracy and efficacy of the method and software are rigorously evaluated using classical benchmarks. The dynamic evolution of cracks in the Koyna dam under seismic loads is accurately reproduced. Furthermore, a thorough assessment of the effects of mesh size and timestep on seismic damage analysis results is conducted, leveraging various engineering focus indicators, culminating in well-founded recommendations for optimal settings.

The paper is organized as follows: Section 2 introduces the theoretical foundation and program implementation of the SBFEM-PFM method. Section 3 assesses the precision and efficiency of the method through two numerical examples. Section 4 conducts a detailed simulation of cracking in the Koyna dam caused by seismic activity, investigating the influence of mesh size and timestep on the analytical results. Conclusively, Section 5 synthesizes the findings and articulates directions for future research.

2. Improved SBFEM-PFM coupled algorithm

2.1. Phase-field equations

The phase-field method utilizes the function $\phi(x)$ to represent fractures in a diffuse manner, as depicted in Fig. 1. The function expression

is as follows:

$$\phi(x) = e^{-\frac{|x-x_I|}{l_0}}, \quad (1)$$

where, l_0 represents the characteristic length. In the phase-field model [33], the crack surface density function is defined as:

$$\gamma(\phi, \nabla\phi) = \frac{1}{2l_0} (\phi^2 + l_0^2 |\nabla\phi|^2). \quad (2)$$

According to the F-M variational principle, introduced by Francfort et al. [34], the total potential energy W is constituted by the bulk strain energy W_e , the external potential energy W_{ext} and the crack surface energy W_d :

$$W = W_e + W_d - W_{ext}. \quad (3)$$

The bulk strain energy W_e , external potential energy W_{ext} , and crack surface energy W_d are defined as follows:

$$W_e = \int_{\Omega} g(\phi) \psi_0(\epsilon) d\Omega, \quad (4)$$

$$W_{ext} = \int_{\Omega} \bar{b} \cdot u d\Omega + \int_{\partial\Omega} \bar{t} \cdot u d\partial\Omega, \quad (5)$$

$$W_d = G_c \int_{\Omega} \gamma(\phi, \nabla\phi) d\Omega, \quad (6)$$

where, $g(\phi)$ denotes the degradation function, $\psi_0(\epsilon)$ represents the nominal strain energy density function, G_c indicates the critical energy release rate, \bar{b} characterizes the body forces, and \bar{t} characterizes the boundary tractions.

The variational derivation of the total potential energy functional $W(u, \phi)$ with respect to the displacement field u and the phase-field ϕ , i.e., $\delta W(u, \phi) = 0$, yields the balance equations for the displacement field and phase-field as follows:

$$\begin{cases} \nabla \sigma + \bar{b} = 0 \\ 2(\phi - 1)\psi(\epsilon) + \frac{G_c}{l_0} (\phi - l_0^2 \nabla^2 \phi) = 0 \end{cases} \quad (7)$$

To prevent the healing of cracks, Miehe et al. [32] introduced the variable H as a substitute for $\psi(\epsilon)$ in Eq. (7) to ensure the irreversibility of cracks. The expression for the variable H is delineated below:

$$H = \max_{t \in (0, T)} \{\psi(\epsilon(x, t))\} \quad (8)$$

2.2. Phase-field scaled boundary finite element

The SBFEM was proposed by Song and Wolf [45–49] and has evolved into a robust method applied across various engineering disciplines. This paper will not expand on the well-documented displacement field SBFEM aspects, focusing instead on the phase-field SBFEM as developed by Hirshikesh et al. [36], which has gained traction within the academic community [62–66].

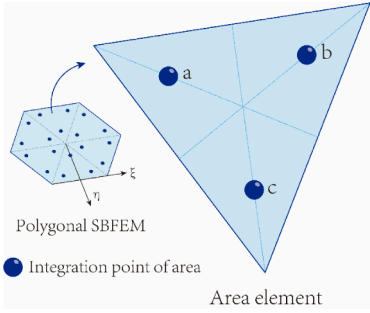
According to Hirshikesh et al. [36], the scaled boundary finite element equation for the phase-field is given by:

$$\begin{aligned} G_c l_0 \left[E_{0\phi} \xi^2 \phi(\xi)_{,\xi\xi} + (E_{0\phi} + E_{1\phi}^T - E_{1\phi}) \xi \phi(\xi)_{,\xi} - E_{2\phi} \phi(\xi) \right] + \left[\frac{G_c}{l_0} + 2H \right] \xi^2 M_{\phi} \\ = \xi^2 P_{\phi}. \end{aligned} \quad (9)$$

The coefficient matrices in the above equation are defined as follows

Table 1

Splitting block Hammer integration scheme.

Integration point diagram	Integration point	Area coordinate	Weight
	a	$\frac{1}{6}, \frac{1}{6}, \frac{2}{3}$	$\frac{1}{6}$
	b	$\frac{1}{6}, \frac{2}{3}, \frac{1}{6}$	$\frac{1}{6}$
	c	$\frac{2}{3}, \frac{1}{6}, \frac{1}{6}$	$\frac{1}{6}$

$$\begin{aligned}
 E_{0\phi} &= \int_{\eta} B_{1\phi}^T(\eta) D B_{1\phi}(\eta) J(\eta) d\eta \\
 E_{1\phi} &= \int_{\eta} B_{2\phi}^T(\eta) D B_{1\phi}(\eta) J(\eta) d\eta \\
 E_{2\phi} &= \int_{\eta} B_{2\phi}^T(\eta) D B_{2\phi}(\eta) J(\eta) d\eta, \\
 M_{\phi} &= \int_{\eta} N_{\phi}^T(\eta) N_{\phi}(\eta) J(\eta) d\eta \\
 P_{\phi} &= 2H \int_{\eta} N_{\phi}^T(\eta) J(\eta) d\eta
 \end{aligned} \quad (10)$$

where $N_{\phi}(\eta)$ represents the shape function matrix for the circumferential line element at the boundary.

The matrices $B_{1\phi}, B_{2\phi}$ in the above equation are given by

$$\begin{aligned}
 B_{1\phi}(\eta) &= b_{1\phi}(\eta) N_{\phi}(\eta) \\
 B_{2\phi}(\eta) &= b_{2\phi}(\eta) N_{\phi}(\eta)_{\eta},
 \end{aligned} \quad (11)$$

where the matrices $b_{1\phi}, b_{2\phi}$ can be calculated as follows:

$$\begin{aligned}
 b_{1\phi}(\eta) &= \frac{1}{J(\eta)} \begin{bmatrix} N_{\phi}(\eta)_{,\eta} y_b \\ -N_{\phi}(\eta)_{,\eta} x_b \end{bmatrix} \\
 b_{2\phi}(\eta) &= \frac{1}{J(\eta)} \begin{bmatrix} -N_{\phi}(\eta) y_b \\ N_{\phi}(\eta) x_b \end{bmatrix}
 \end{aligned} \quad (12)$$

The second-order differential equation, Eq. (9), is transformed into a first-order ordinary differential equation by introducing the Hamiltonian matrix as follows:

$$Z_{\phi} V_{\phi} = V_{\phi} \Lambda_{\phi}. \quad (13)$$

Hamiltonian matrix Z_{ϕ} is given by

$$Z_{\phi} = \begin{bmatrix} (E_{0\phi})^{-1} (E_{1\phi})^T & -(E_{0\phi})^{-1} \\ E_{1\phi} (E_{0\phi})^{-1} (E_{1\phi})^T - E_{2\phi} & -E_{1\phi} (E_{0\phi})^{-1} \end{bmatrix}. \quad (14)$$

Upon performing an eigenvalue decomposition or Schur decomposition on the Hamiltonian matrix Z_{ϕ} [69], eigenvalues Λ_{ϕ} and eigenvectors V_{ϕ} are derived:

$$\Lambda_{\phi} = \begin{bmatrix} \Lambda_{\phi}^+ & 0 \\ 0 & \Lambda_{\phi}^- \end{bmatrix}, \quad (15)$$

$$V_{\phi} = \begin{bmatrix} V_{\phi 11} & V_{\phi 12} \\ V_{\phi 21} & V_{\phi 22} \end{bmatrix}. \quad (16)$$

According to relevant theory, the general solution for Eq. (9) can be derived as follows:

$$\phi(\xi) = V_{\phi 11} \xi^{-\Lambda_{\phi}} V_{\phi 11}^{-1} \phi_b. \quad (17)$$

The phase-field $\phi(\xi, \eta)$ at any internal point within a scaled boundary finite element can be computed based on the phase-field ϕ_b at the circumferential boundary nodes, according to the equation presented below:

$$\phi(\xi, \eta) = \mathbb{N}_{\phi}(\xi, \eta) \phi_b. \quad (18)$$

At the same time, the polygon element shape function $\mathbb{N}_{\phi}(\xi, \eta)$ is extracted as

$$\mathbb{N}_{\phi}(\xi, \eta) = N_{\phi}(\eta) V_{\phi 11} \xi^{-\Lambda_{\phi}} V_{\phi 11}^{-1}. \quad (19)$$

Similarly, the gradient of the phase-field is defined as

$$\nabla \phi(\xi, \eta) = B_{1\phi}(\eta) \phi(\xi)_{,\xi} + \xi^{-1} B_{2\phi}(\eta) \phi(\xi). \quad (20)$$

Substituting Eq. (18) into Eq. (20) yields the derivative matrix of the phase-field shape function

$$\mathbb{B}_{\phi}(\xi, \eta) = \left[B_{1\phi}(\eta) V_{\phi 11} \left(-\Lambda_{\phi}^+ \right) + B_{2\phi}(\eta) V_{\phi 11} \right] \xi^{-\Lambda_{\phi}^+ - I} V_{\phi 11}^{-1}. \quad (21)$$

The circumferential numerical and radial analytical properties of the SBFEM provide high precision and the flexibility to construct polygonal elements. However, accurately obtaining the phase-field values within elements remains challenging. Researchers hypothesized that the phase-field within an element corresponds to the nodal average phase-field [36,62-66]. This hypothesis implies that all phase-field-related variables remain constant within the element, thus limiting the variability in the internal phase-field. Furthermore, this assumption is linked to the size constraints of discrete geometries in the regularized phase-field model, where the mesh size must represent the size of the crack [36], imposing stringent requirements on mesh size.

In terms of nonlinear applications of SBFEM, a nonlinear solution methodology for SBFEM based on analytical integration was proposed by Ooi et al. [70], which tackled the challenges associated with nonlinear applications of SBFEM. However, this approach requires smaller element sizes and involves a complex procedural framework, limiting its practicality for broad engineering analyses. Following this, Chen et al. [71] developed an accessible and efficient nonlinear SBFEM approach, utilizing constant stiffness characteristic eigenvalue decomposition and subdomain Hammer integration techniques, pushing forward its application in nonlinear geotechnical engineering.

To overcome the limitations of conventional SBFEM-PFM, the subdomain block Hammer integration is introduced for calculating the phase-field within element. The block Hammer integration approach adopted in this study (as detailed in Eq. (22)) places three integration points within each triangular zone corresponding to each

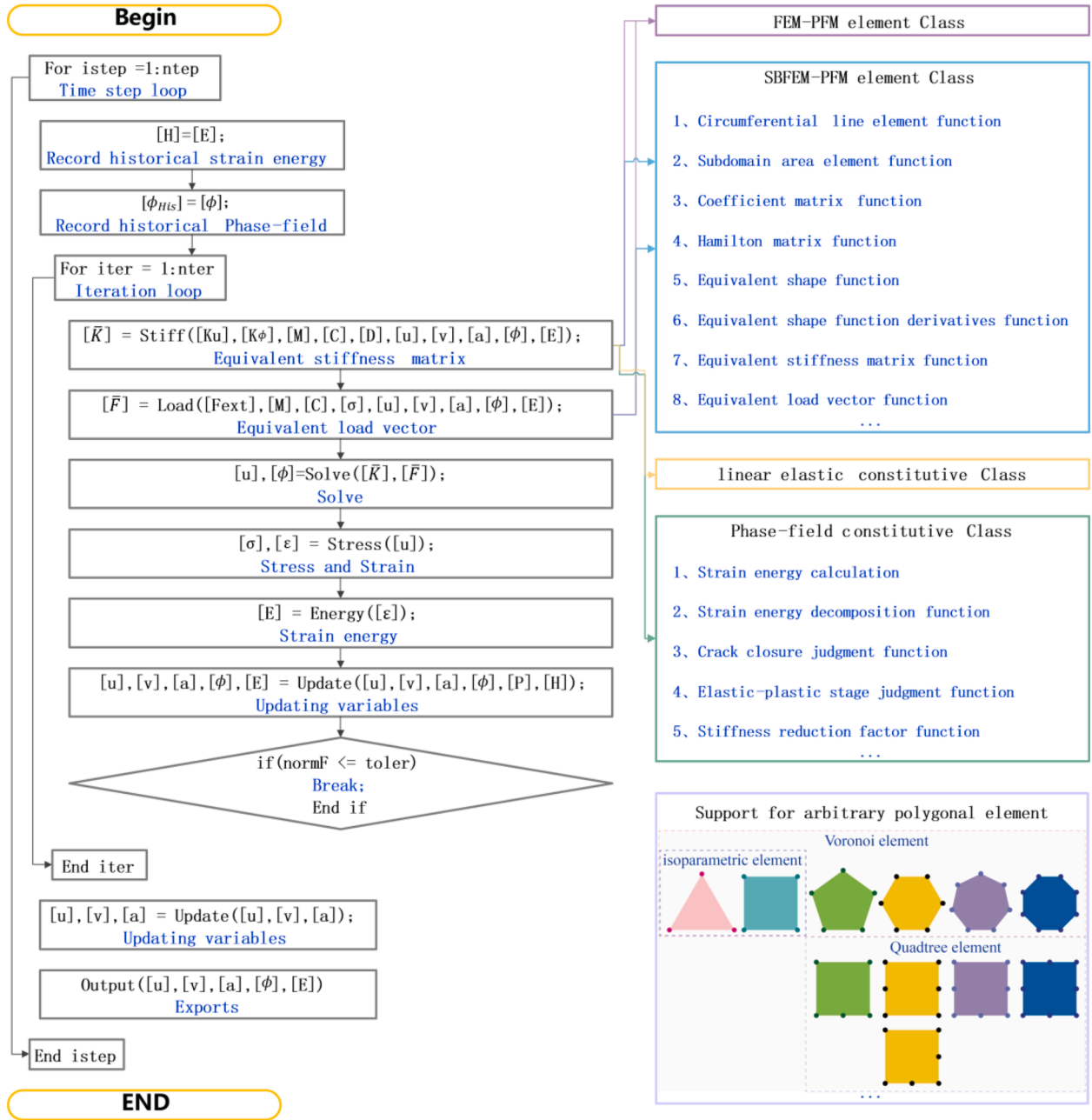


Fig. 2. Program implementation framework and information of critical classes.

circumferential boundary line element, with specific coordinates and integration weights provided in Table 1

$$\int_{\Omega_e} f(\xi, \eta) d\xi d\eta = \frac{1}{6} \left[f\left(\frac{2}{3}, \frac{1}{6}\right) + f\left(\frac{1}{6}, \frac{2}{3}\right) + f\left(\frac{1}{6}, \frac{1}{6}\right) \right] + o, \quad (22)$$

By performing integration across these points, the stiffness matrices for both the displacement and phase-field are derived with the equations as follows:

$$K_u^e = \sum_{s=1}^{3n} [(1 - \phi_s)^2 + k] (\mathbb{B}_u(\xi, \eta))^T D \mathbb{B}_u(\xi, \eta) A_s, \quad (23)$$

$$K_\phi^e = \sum_{s=1}^{3n} \left\{ \left[\frac{G_c}{l_0} + 2H(\varepsilon) \right] (\mathbb{N}_\phi(\xi, \eta))^T \mathbb{N}_\phi(\xi, \eta) + G_c l_0 (\mathbb{B}_\phi(\xi, \eta))^T \mathbb{B}_\phi(\xi, \eta) \right\} A_s, \quad (24)$$

where s represents the number of integration points and n represents the edge number of the 2D polygonal element, and the total number of integration points for a scaled boundary finite element is $3n$.

Similarly, by integrating over the area integration points, the internal force vectors for the displacement field and the phase-field can be obtained as follows:

$$R_u^e = \sum_{s=1}^{3n} [(1 - \phi_s)^2 + k] (\mathbb{B}_u(\xi, \eta))^T \sigma_s A_s, \quad (25)$$

$$R_\phi^e = \sum_{s=1}^{3n} \left\{ \left[\frac{G_c}{l_0} \phi_s - 2(1 - \phi_s) H_s(\varepsilon) \right] (\mathbb{N}_\phi(\xi, \eta))^T + G_c l_0 (\mathbb{B}_\phi(\xi, \eta))^T \nabla \phi_s \right\} A_s. \quad (26)$$

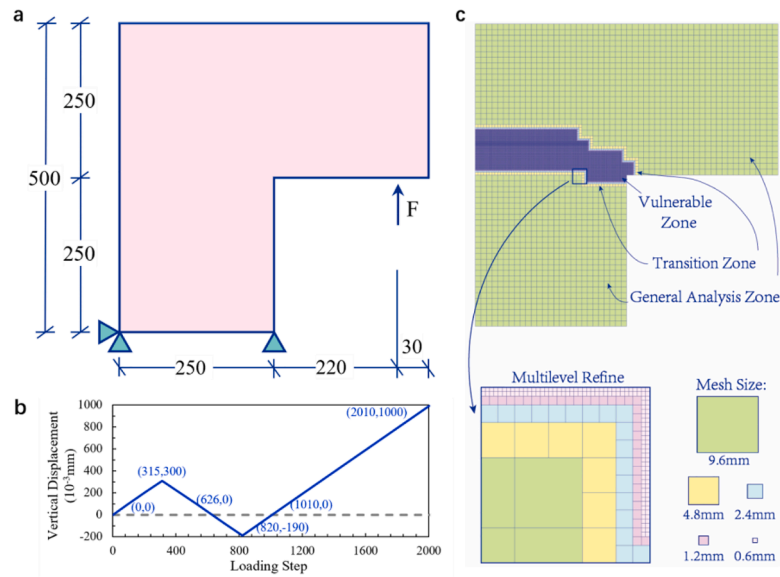


Fig. 3. (a) Geometry and boundary conditions (unit: mm), (b) Loading curve, and (c) Mesh and local refinement.

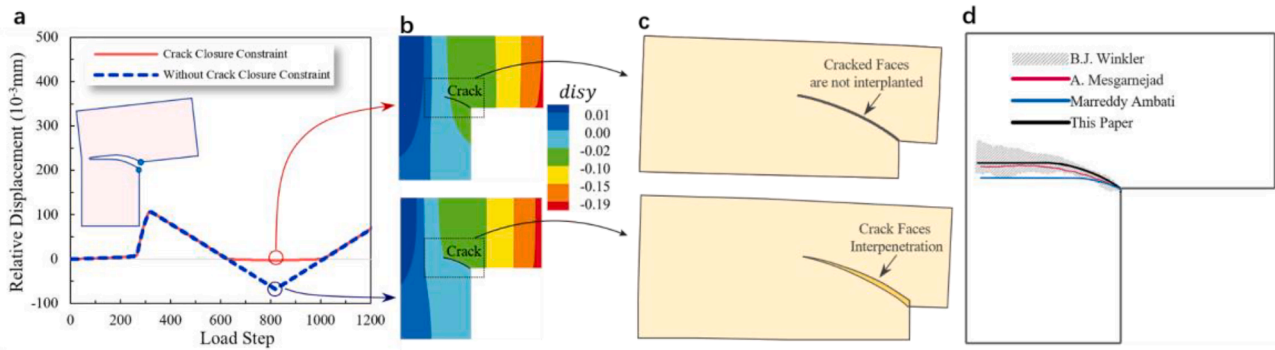


Fig. 4. L-shaped component test. (a) Relative displacement on both sides of the crack-load step curves, (b) Vertical displacement, (c) Geometric deformation, and (d) Comparison of the final crack with other researchers [72,81,82].

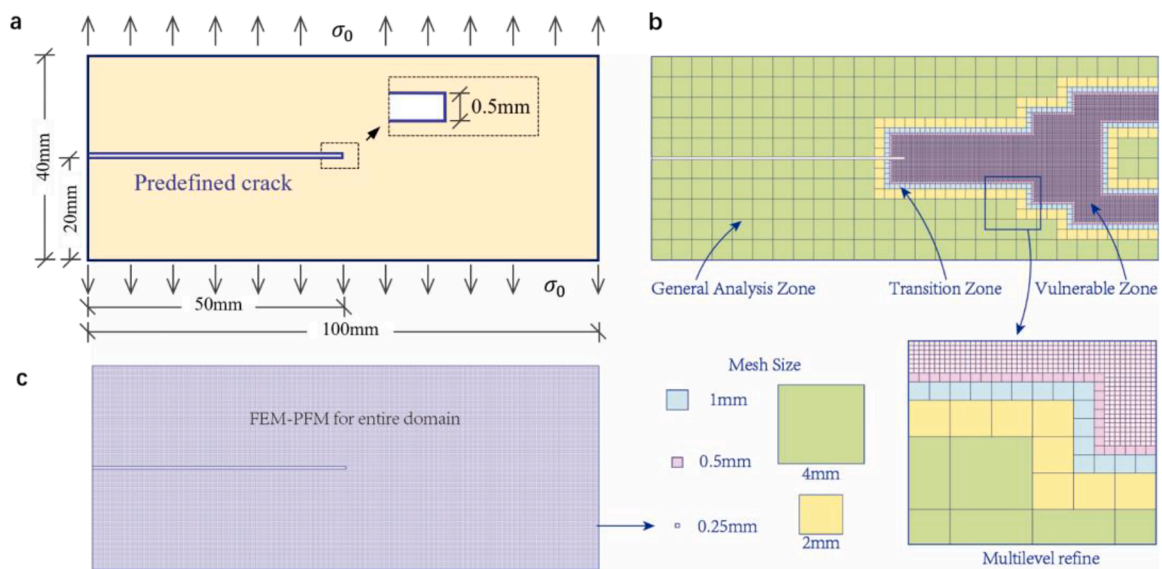


Fig. 5. Geometry and meshing (a) Geometry and boundary conditions, (b) Mesh of synergistic coupling of PFM-elasticity with SBFEM-FEM, (c) Uniform fine-scale mesh across the entire component.

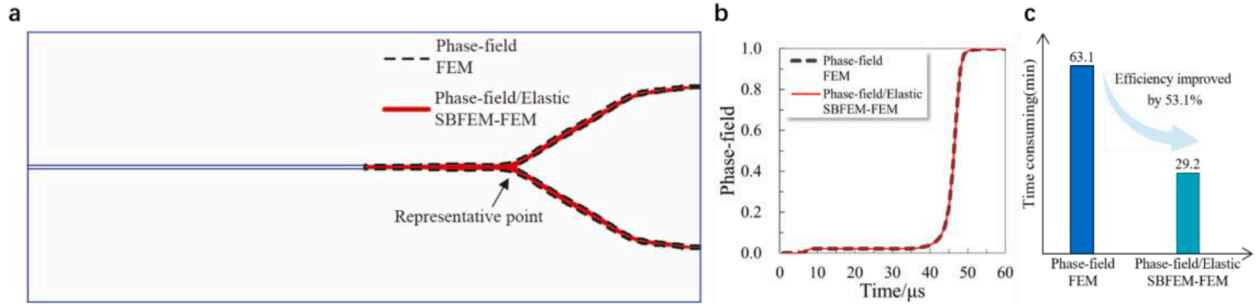


Fig. 6. Calculation results, and time-consuming. (a) Phase-field results of $t = 90 \mu s$. (b) Representative point phase-field - time curve. (c) Time-consuming of the two schemes.

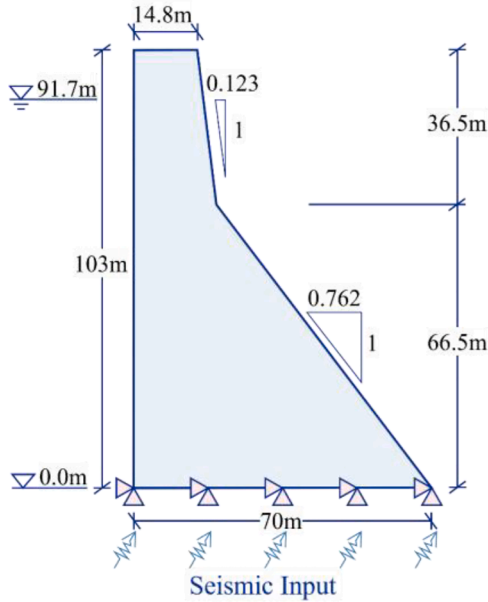


Fig. 7. Geometry and boundary conditions.

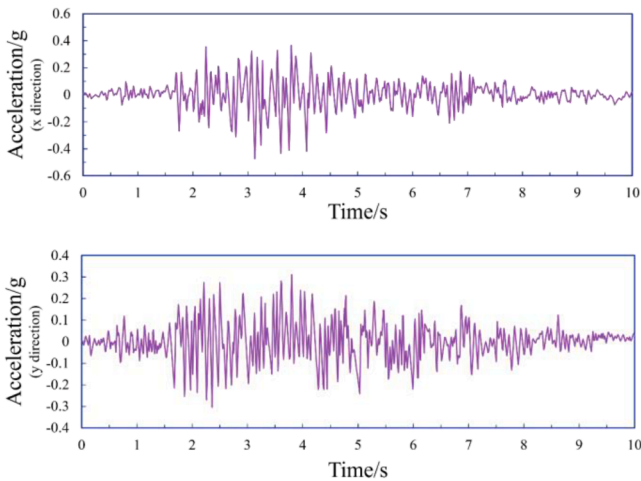


Fig. 8. Ground vibration input curve.

2.3. Closure constraints for reciprocal load

As devised by Ambati et al. [72], the "closure constraint" method is adopted for analyzing phase-field under reciprocal load in this paper. This method prevents crack face interpenetration by setting the

phase-field ϕ to zero when the compressive strain energy ψ^- exceeds the tensile strain energy ψ^+ , as described:

$$\forall x: \psi^- > \psi^+ \Rightarrow \phi = 0. \quad (27)$$

The implementation details are as follows: the recorded phase-field ϕ remains unchanged, and the degradation function is reset to 1 for any point within the domain where the compressive strain energy ψ^- exceeds the tensile strain energy ψ^+ . Additionally, the phase-field internal force R_ϕ is set to 0. In simpler terms, this degrades the phase-field element to the finite element.

2.4. Threshold strategy for preventing initial stiffness decay

The traditional AT2 model's failure criterion is activated immediately upon loading, leading to a rapid degradation of stiffness without an initial elastic phase [73]. This behavior creates a mismatch with the characteristics of modern engineering materials. To resolve these issues, this paper has embraced the threshold strategy proposed by Yu et al. [74]. The AT2 model is enhanced by this strategy through the incorporation of a linear elastic stage, thereby averting the premature onset of damage. Such enhancements make the model's predictions more closely match actual conditions, improving the rationality and reliability of PFM applications. The refinements include revising the crack surface density function and establishing a threshold based on the historical maximum strain energy. These adjustments are detailed in the equations below:

$$\gamma(\phi, \nabla \phi) = \frac{1}{2l_0} (\phi + \phi_s)_+^2 + \frac{l_0}{2} |\nabla \phi|^2, \quad (28)$$

$$H(x, t) = \max \left\{ \psi^+, \frac{\phi_s G_c}{2l_0} \right\}. \quad (29)$$

Following the implementation of the aforementioned improvements, the elastic critical strain and stress of the material are as shown in the following equations:

$$\varepsilon = \sqrt{\frac{G_c}{3El_0}}, \quad (30)$$

$$\sigma = \sqrt{\frac{EG_c}{3l_0}}. \quad (31)$$

2.5. Program framework design and integration

Seismic analysis of large structures involves intricate challenges, including multi-field coupling, discontinuous deformation, strong nonlinearity, and a broad span of mesh sizes. These complexities often exceed the capabilities of traditional numerical methods alone. The well-established FEM offers stability and efficiency. SBFEM, supporting complex polygonal elements, facilitates cross-scale refined calculation.

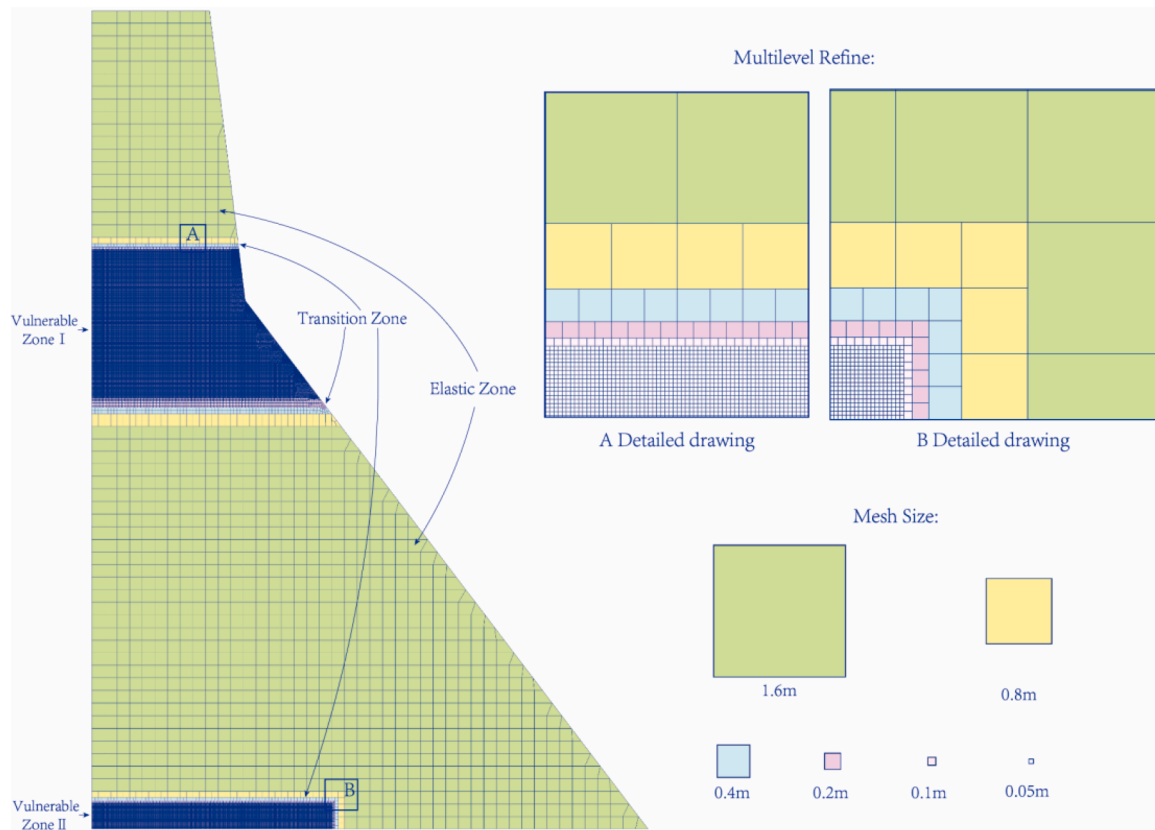


Fig. 9. Mesh and local magnification (unit: m).

Meanwhile, the PFM automatically determines crack paths, obviating the need for initial fracture criteria. By integrating diverse computational approaches, their strengths can be combined to develop a robust strategy for assessing seismic damage in large-scale engineering projects.

2.5.1. Software integration platform

Since the early 1990s, supported by a series of national-level grants, the authors' team has been dedicated to the independent development of GEODYNA [75], a comprehensive geotechnical engineering software system comprising over 300,000 lines of code. The principal features of this system are outlined as follows:

- ① It integrates a suite of consistent command input methods, element activation techniques, strain potential actions, time integration methods, and strength reduction approaches, facilitating comprehensive analyses of processes including filling, excavation, wetting, creep, seismic permanent deformations, consolidation, dynamics, and stability. This integration has culminated in a unified software development model tailored for large-scale geotechnical engineering.
- ② Engineered on the Visual Studio C++ platform and MFC environment, GEODYNA leverages object-oriented design principles such as type abstraction, inheritance, overloading, and polymorphism. This design ethos encapsulates and refines types essential for finite element analysis, including material constitutive models, pore water seepage models, seismic pore water pressure models, element types, load types, and solvers, thereby establishing a potent class library for finite element analysis in geotechnical engineering.
- ③ The software assimilates leading research on the seismic destruction of major geotechnical structures, notably high earth-rock dams. It incorporates advanced models such as the generalized plasticity model for rockfill materials, the plastic damage model for

concrete, the three-dimensional elastoplastic model for interfaces, and seismic wave input methods. These features enable a meticulous full-process numerical simulation analysis of the failure mechanisms in large-scale geotechnical engineering.

GEODYNA, equipped with a suite of numerical analysis methods including FEM, SBFEM, and PFM, along with user-friendly secondary development interfaces, serves as a foundational tool for algorithm integration in this study.

2.5.2. Program framework and implementation

In accordance with object-oriented programming principles, the shared properties of the FEM-PFM and SBFEM-PFM configurations are generalized in the section. The standardized member functions, external interfaces, and internal inheritance hierarchies are established to harmonize the implementation of diverse elements within the program. The programming architecture and critical class libraries are illustrated in Fig. 2.

Inheriting the capabilities of GEODYNA, the integrated SBFEM-PFM and FEM-PFM algorithms benefit from multicore parallel processing and efficient GPU-based solutions. Furthermore, convenient utilization of extensive material constitutive libraries, load databases, and post-processing components is enabled by the integrated program, providing strong technical support for conducting detailed fracture analyses of structures under severe seismic conditions.

2.5.3. Time integration

Selecting an appropriate dynamic time integration method is crucial for ensuring calculation accuracy, efficiency and stability. The Newmark integration method, widely used in seismic analyses of large engineering structures, is supported by extensive practical experience. The description of the integration process is presented below.

For any arbitrary domain, the dynamic equilibrium equation of the

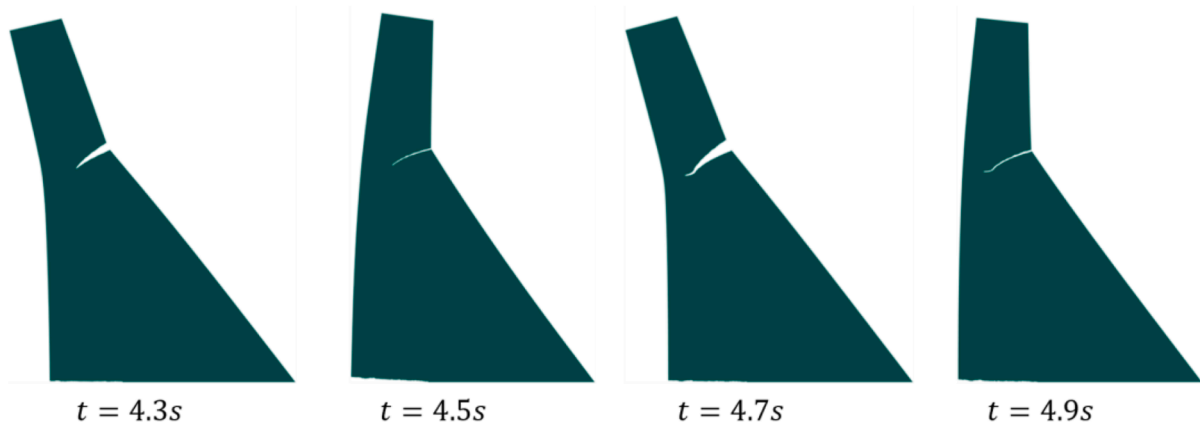
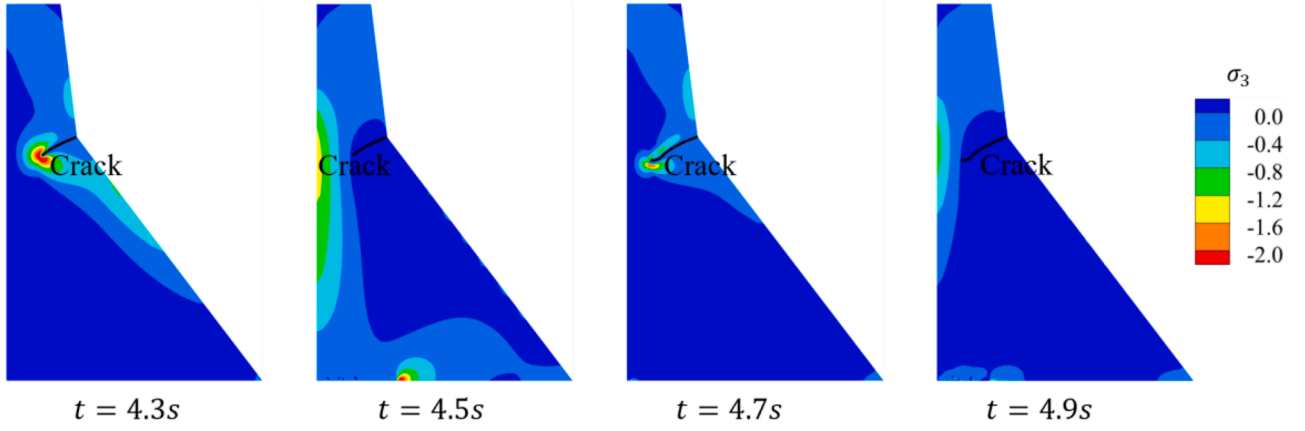
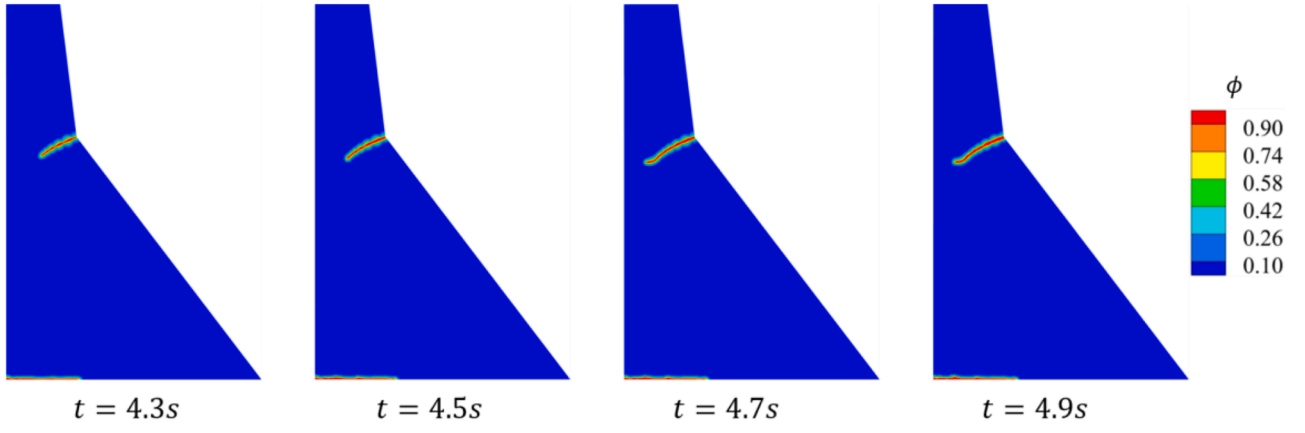


Fig. 10. The phase-field, minor principal stress, and dam deformation of critical moments.

undamped displacement field is:

$$Ma + K_u(\phi)x = F(t) \quad (32)$$

For seismic evaluations, the damping matrix is typically constructed using the Rayleigh damping theory proposed by Idriss [76], as follows:

$$C = aM + bK, \quad (33)$$

where, a and b are the damping constants.

Substituting Eq. (33) into Eq. (32) yields

$$Ma + Cv + K_u(\phi)x = F(t) \quad (34)$$

Real-world earthquakes, which generally last between 10 seconds to one minute, feature varying frequencies and large amplitude fluctuations. To manage these, implicit time integration schemes, which allow for larger time step, are utilized. Consequently, the generalized

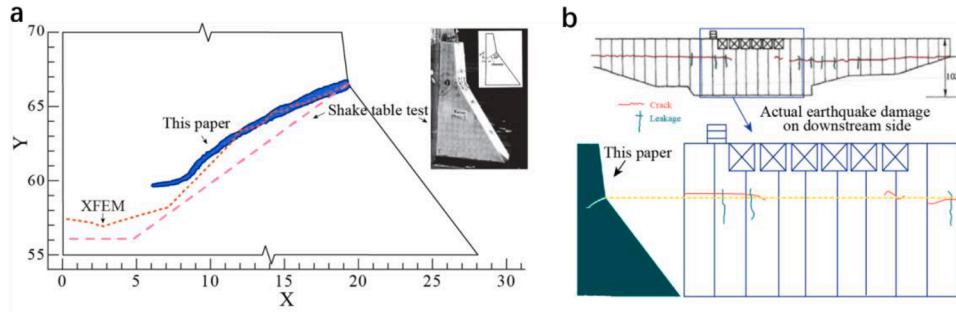


Fig. 11. Comparison of results. (a) Comparison of results from the proposed method with XFEM [28,99] and shake table test [100]. (b) Comparison of results from the proposed method with the actual seismic damage [101].

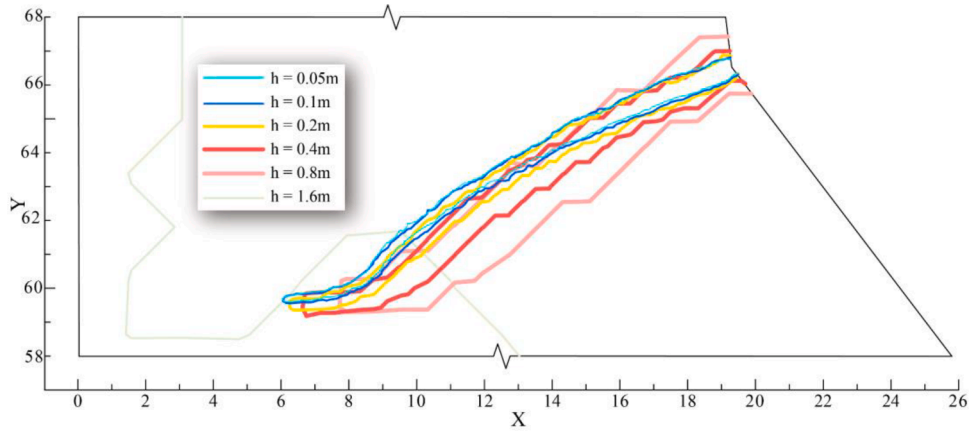


Fig. 12. Phase-field contour near vulnerable zone I ($\phi = 0.95$).

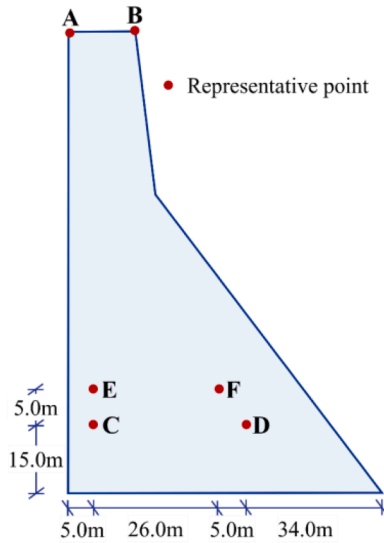


Fig. 13. Representative point location.

Newmark method [77] is employed for dynamic implicit time integration. The dynamic equilibrium equation for the displacement field is as follows:

$$\bar{K}_u \{u\}_{n+1} = \bar{R}_u, \quad (35)$$

where the equivalent stiffness matrix and equivalent load matrix are as follows:

$$\begin{cases} \bar{K}_u = K_u(\phi) + \frac{1}{\beta \Delta t^2} M + \frac{\alpha}{\beta \Delta t} C \\ \bar{R}_u = -M \{a_s\}_{n+1} + M \{A\}_n + C \{B\}_n + \int_{\Omega} B \sigma dV \end{cases} \quad (36)$$

In the above equation, α and β are constants of time integration.

While conducting dynamic time integration of the displacement field, the phase-field equations are solved. As the displacement and phase-fields are coupled in a nonlinear framework, iterative methods become crucial to accurately solve the coupling system.

2.5.4. Monolithic iterative solution

The coupled equations are tackled through the monolithic iterative strategy. To enhance the efficiency of the solution scheme, the interaction between fields is disregarded, leading to the elimination of the off-diagonal matrices $K_{u\phi}$ and $K_{\phi u}$. This method is corroborated by findings from [78–80]. The specific iterative protocol is delineated below:

$$\begin{Bmatrix} u \\ \phi \end{Bmatrix}_{n+1} = \begin{Bmatrix} u \\ \phi \end{Bmatrix}_n + \begin{bmatrix} \bar{K}_u & \\ & K_\phi \end{bmatrix}_n^{-1} \begin{Bmatrix} \bar{R}_u \\ R_\phi \end{Bmatrix}_n. \quad (37)$$

3. Validation of accuracy and efficiency

The accuracy and efficiency of the proposed method are validated in this section. The failure process of the L-shaped component under static reciprocal loading is examined in Section 3.1, where computational results are compared with experimental data to confirm the method's precision. A classic dynamic crack branching example is employed in Section 3.2 to evaluate the computational efficiency of the proposed method. Together, these two examples provide a comprehensive assessment of the method's performance and reliability, forming a solid

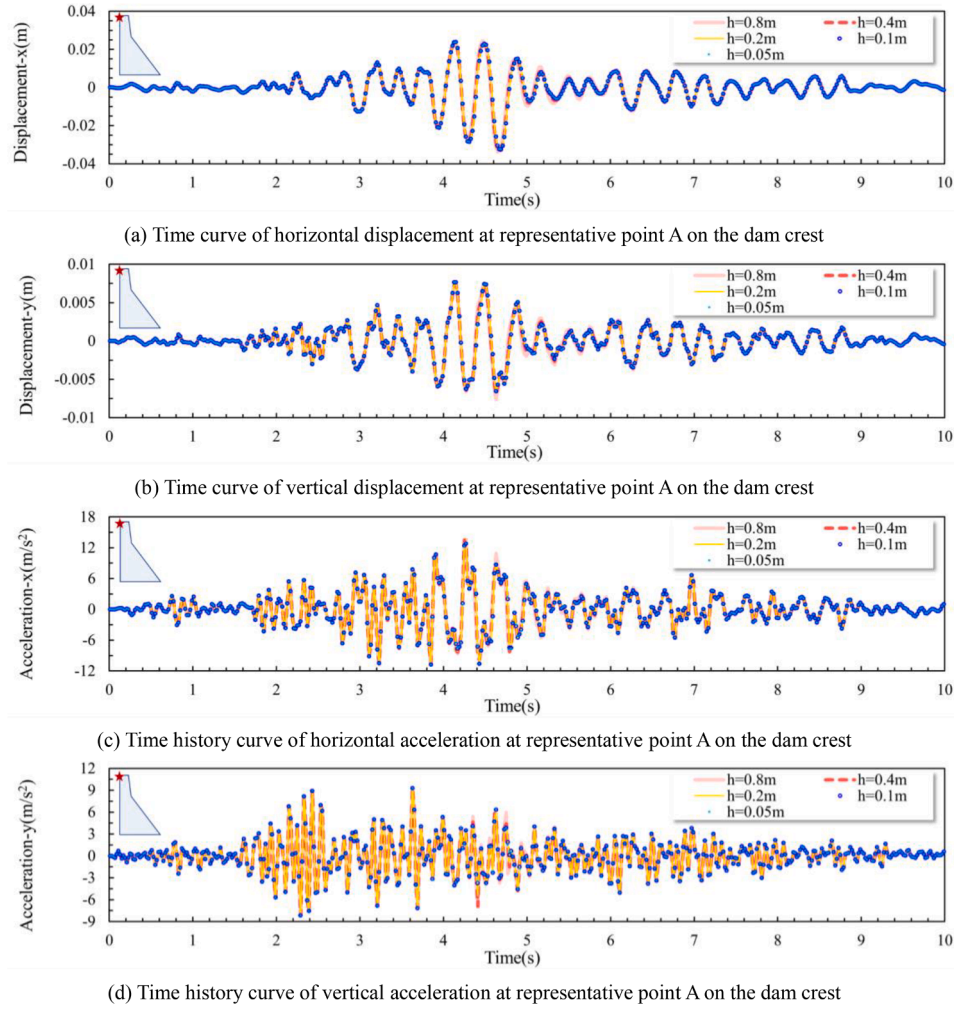


Fig. 14. Time history curve at representative point A on the dam crest.

foundation for its application in engineering structures.

3.1. L-shaped component test

The widely recognized L-shaped component failure tests [72,81–86] are employed in this section as a benchmark for validation. The universally recognized cracking patterns serve to objectively assess the proposed method, enhancing the credibility of the validation efforts and reinforcing the method's reliability.

3.1.1. Geometry and boundary conditions

The specimen's geometry and boundary conditions are depicted in Fig. 3a, featuring external dimensions of 500 mm and internal dimensions of 250 mm, with the bottom secured as a fixed constraint. Displacement loads are applied as marked on the diagram, with a detailed load curve presented in Fig. 3b.

3.1.2. Mesh discretization

The discretized model is presented in Fig. 3c, which employs polygonal transition elements and a mesh refinement strategy that progressively refines the mesh size in vulnerable zones from 9.6 mm to 0.6 mm. The model consists of 49,433 nodes and 48,729 SBFEM-PFM coupling elements.

3.1.3. Material parameters

The material parameters utilized in this study are derived from the research conducted by Ambati et al. [72] and Mesgarnejad et al. [81].

The specific values adopted are elastic modulus (E) = 25.84 GPa, Poisson's ratio (ν) = 0.18, critical energy release rate (G_c) = 89 N/m, and characteristic length (l_0) = 1.1875 mm.

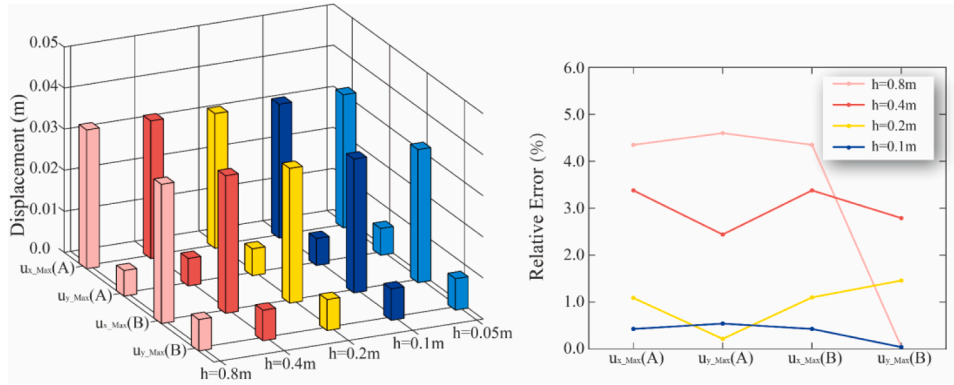
3.1.4. Analysis of computational results

Two scenarios are presented for comparison: one incorporating the closure constraint and the other without. This comparison evaluates the importance of preventing crack face interpenetration.

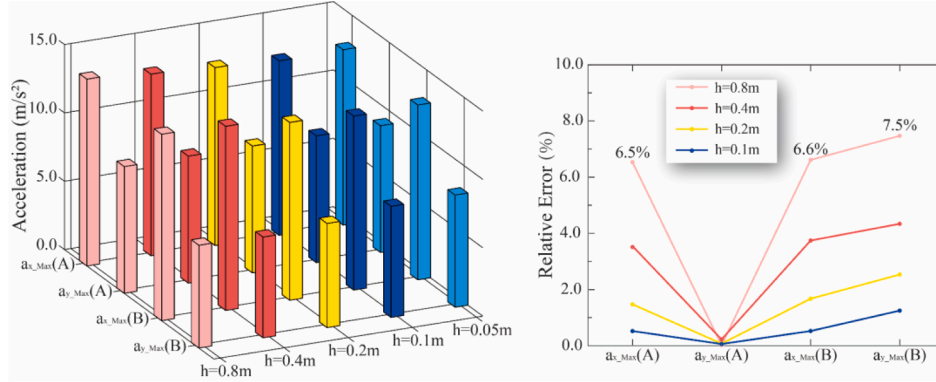
The relative displacements of the nodes flanking the crack are depicted in Fig. 4 (a). When the crack is closed, only compressive elastic deformation is observed near the closed crack due to the restoration of stiffness. As the load reaches its reverse peak, the vertical displacements are depicted in Fig. 4 (b), and the geometric deformations are presented in Fig. 4 (c). The analysis demonstrates the crucial function of closure constraints in preventing the interpenetration of crack surfaces, which is essential for attaining more precise and realistic computational outcomes. The final crack pattern is shown in Fig. 4 (d). The distribution of crack in this study closely matches the simulation results of Mesgarnejad et al. [81] and Ambati et al. [72], and aligns with the experimental failure zone identified by Winkler [82]. These findings confirm that the software developed in this study is competent for analyzing the structural damage process under reciprocal loading.

3.2. Dynamic crack branching

A classic dynamic crack branching benchmark, extensively utilized in the phase-field fracture domain [87–96], is employed to assess the



(a) Maximum displacement and relative errors over the entire duration at representative points A and B



(b) Maximum acceleration and relative errors over the entire duration at representative points A and B

Fig. 15. Maximum displacement and acceleration values and relative errors over the entire duration of representative points at the dam crest.

efficiency of the proposed method.

3.2.1. Geometry and boundary conditions

The rectangular component measuring 100 mm by 40 mm, featuring a pre-existing 50 mm crack on the left side, as illustrated in Fig. 5 (a). At the initial moment ($t=0s$), a uniform step load of 1 MPa is applied to both the upper and lower boundaries of the component.

3.2.2. Mesh discretization

Two distinct mesh configurations were established to evaluate the efficacy of the proposed method. The first configuration, shown in Fig. 5 (b), employs a cross-scale discretization approach integrating polygonal transition elements and gradually refines the mesh from 4.0 mm to 0.25 mm in zones expected to experience high stress. The model includes 11,188 nodes, with the transition and vulnerable zones precisely modeled using phase-field elements (568 elements coupling with SBFEM and 10,048 with FEM). The second configuration, depicted in Fig. 5(c), applies a uniform fine-scale mesh across the entire component, consisting of 63,602 PFM-FEM elements.

3.2.3. Material parameters

In accordance with the previous studies [87–96], the material properties are defined as follows: Young's modulus (E) is 32.0GPa, Poisson's ratio (ν) is 0.2, the critical energy release rate (G_c) is 3 N/m, and the characteristic length (l_0) is 0.50 mm.

3.2.4. Analysis of computational results

Two computational schemes are established to assess the efficiency of the synergistic coupling of PFM-elasticity with SBFEM-FEM strategies. The final phase-field distributions for both models are presented in Fig. 6a, while the phase-field evolution over time at representative

points is presented in Fig. 6b. Fig. 6c provides a comparison of the computational times. The results demonstrate that the synergistic coupling scheme not only maintains precision but enhances computational efficiency by 53.1%. The synergistic coupling scheme is applied consistently in the following examples.

4. Engineering applications and discussion

In Section 4.1, the proposed method is employed to reproduce the catastrophic process of the Koyna dam during seismic events. The effects of mesh size and timestep on the simulation results are further investigated in Section 4.2. These efforts are designed to affirm the dependability and suitability of the proposed method for dynamic fracture analysis in substantial structures, offering pertinent recommendations for engineering applications.

4.1. Koyna earthquake disaster production

Located on the Koyna river in India, the Koyna concrete gravity dam stands 103 meters tall. In 1967, the dam sustained severe damage from a strong 6.5 magnitude earthquake, which led to cracks in the structure. As one of the few gravity dams with detailed records of damage from a major seismic event, the Koyna dam is widely referenced as a benchmark model for studying the seismic failure behavior of gravity dams.

4.1.1. Geometry and boundary conditions

The proposed method was employed to replicate seismic disasters of the Koyna gravity dam. The geometric configuration and constraints of the dam are depicted in Fig. 7 with a height of 103 meters and a maximum reservoir water level of 91.7 meters. Under static conditions, the dam is primarily subjected to its own weight and the hydraulic

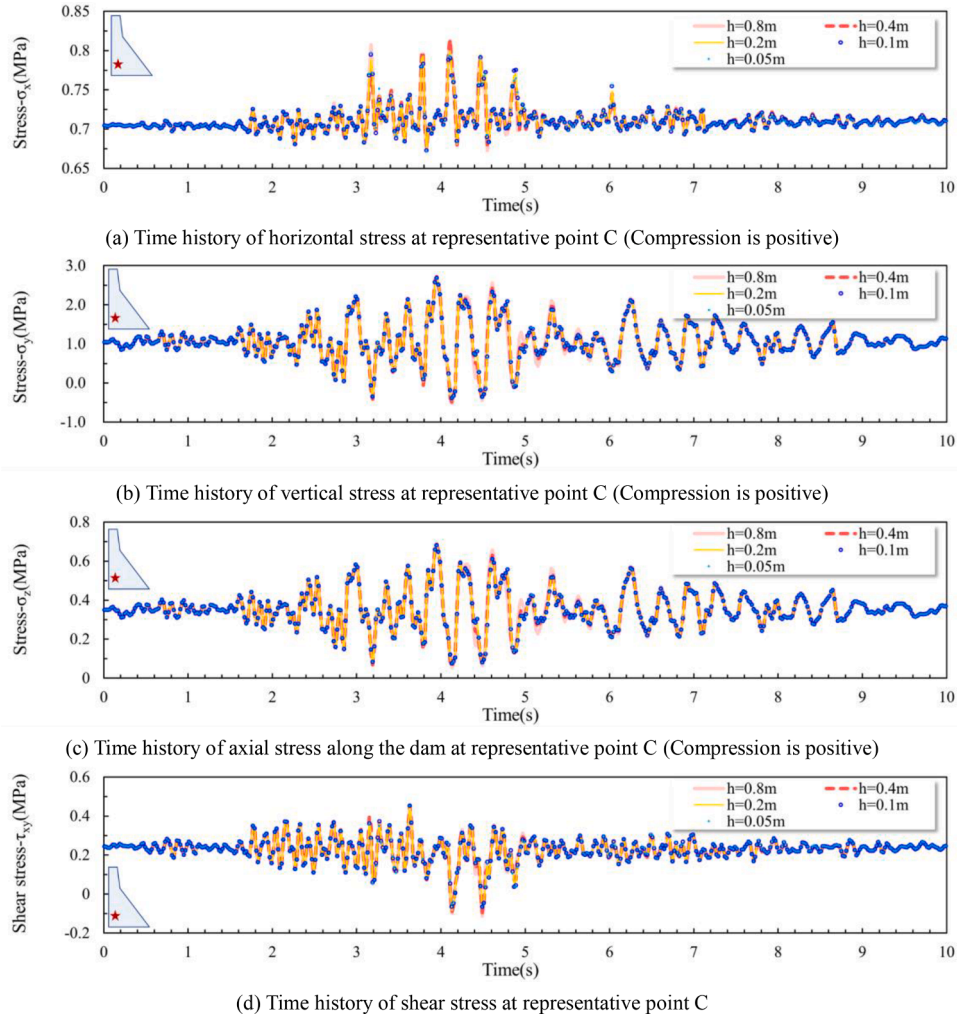


Fig. 16. Stress time history curves at representative point C.

pressure from the upstream water. The seismic data employed in the simulation characterizes a maximum horizontal ground acceleration of 0.49g along with a vertical acceleration of 0.34g, as shown in Fig. 8. The hydrodynamic pressure effects were considered using the added mass method [97].

4.1.2. Mesh discretization

The computational model is shown in Fig. 9, which utilizes polygonal transition elements and a progressive mesh refinement strategy to refine the mesh size in the vulnerable zones from 1.6m to 0.05m. The model encompasses 216,736 nodes. The transition and vulnerable zones are built with phase-field elements (1,599 elements coupling with SBFEM and 212,445 with FEM), whereas the elastic zone is discretized by 1,103 isotropic elastic elements.

4.1.3. Material parameters

The concrete material parameters of the Koyna dam are as follows: the density (ρ) of 2.63 g/cm³, the elastic modulus (E) of 31GPa, the Poisson's ratio (ν) of 0.2, the critical energy release rate (G_c) of 325N·m, and the characteristic length (l_0) of 0.4 m. Damping calculations employed Rayleigh damping with a damping ratio set to 5% [98], and the time step is 0.005s.

4.1.4. Analysis of computational results

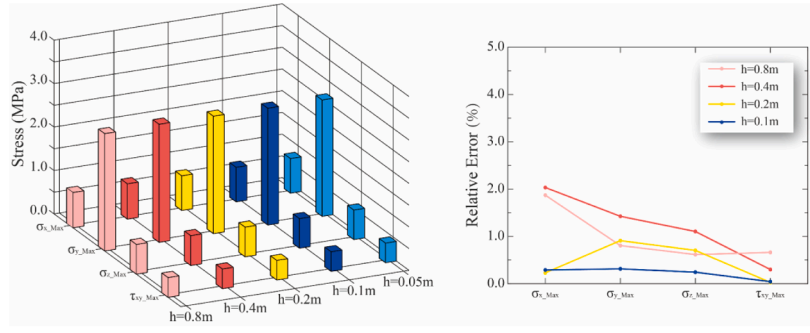
The phase-field, minor principal stress, and dam deformation at critical time steps ($t=4.3s$, $4.5s$, $4.7s$, and $4.9s$) are illustrated in Fig. 10.

At 4.3s, a significant crack opening occurs near the turning point of the downstream dam slope, which then closes by 4.5s due to the influence of seismic loads and inertial forces. The crack reopens at 4.7s, extending further, and closes again at 4.9s. As illustrated in Fig. 10b, at $t=4.3s$ and $4.7s$, the notable tensile stress concentration is observed at the crack tips.

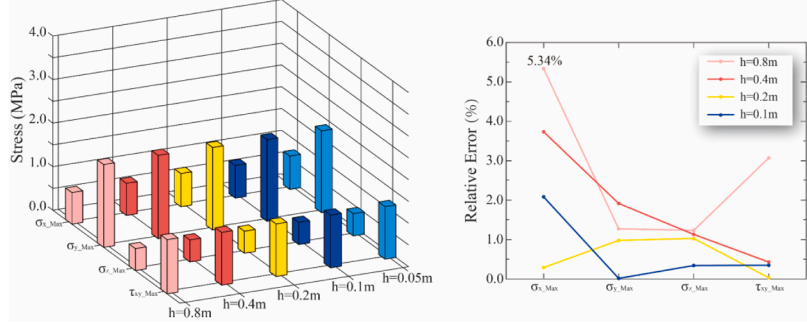
The results obtained from the proposed method are compared with those from XFEM [28,99] and shake table tests [100], as shown in Fig. 11a. Additionally, Fig. 11b highlights the actual seismic damage observed near the turning point of the downstream dam slope [101]. Horizontal cracks in water-retaining dam segments align closely with the crack paths calculated in this paper. Comparisons with other numerical methods, experimental data, and real seismic damages have substantiated the applicability of the method introduced in this paper for seismic analysis of dams.

4.2. Exploration of parameters in practical applications

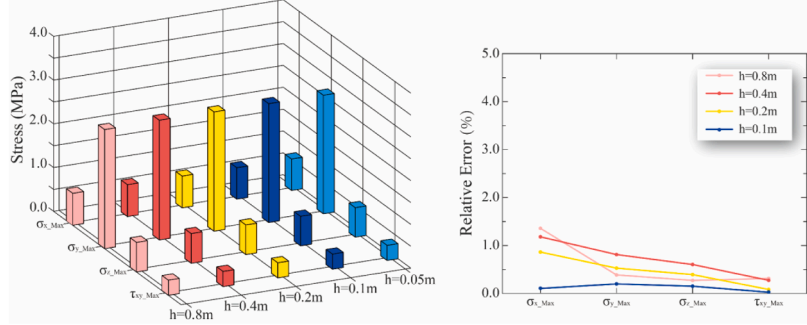
This section delves into determining the optimal mesh size and timestep, which are critical for maintaining computational stability and accuracy when using the phase-field method. The effects of mesh sizes and timesteps on key metrics such as structural dynamic displacement, acceleration, and stress across multiple scenarios are investigated in this section. Based on these analyses, practical analytical parameters are recommended to serve as references for seismic fracture simulations in similar engineering projects.



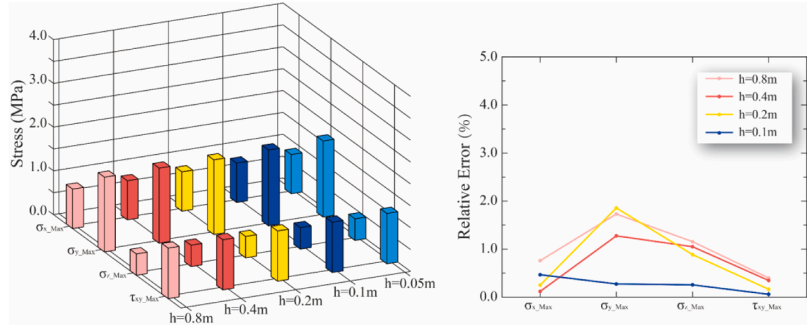
(a) Maximum dynamic stress over the entire duration and the relative error at representative point C



(b) Maximum dynamic stress over the entire duration and the relative error at representative point D



(c) Maximum dynamic stress over the entire duration and the relative error at representative point E



(d) Maximum dynamic stress over the entire duration and the relative error at representative point F

Fig. 17. Maximum dynamic stress values and relative errors over the entire duration at representative points.

4.2.1. Mesh size

In the phase-field model, fractures are described using a field variable that changes rapidly near fractures. Oversized mesh sizes may skew simulation results and lead to computational instability. Therefore, it is crucial to choose a mesh size that guarantees accurate simulation outcomes. Existing studies [33,73] suggest that mesh sizes $h < 0.2 \sim 0.5l_0$ produce relatively accurate measurements of crack areas. However, the specific effects of mesh size at the fracture on the seismic response of

large structures remain unclear.

In this section, numerical models with six distinct mesh densities are employed to investigate the influence of mesh size on the seismic responses of large structures. The evaluated mesh sizes are 1.6 m, 0.8 m, 0.4 m, 0.2 m, 0.1 m, and 0.05 m. The final crack distribution near the turning point of the downstream dam slope, calculated by the six distinguish mesh schemes, is presented in Fig. 12. The results demonstrate that the $h=1.6m$ mesh size is inadequate for accurately

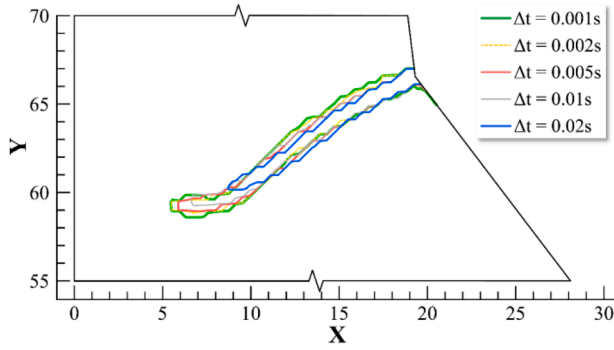


Fig. 18. Contour lines of the phase-field at the last moment for different timestep schemes ($\phi=0.95=0.95$).

representing crack morphology. In contrast, the $h=0.8\text{m}$ mesh size provides a more precise depiction, particularly in the capturing of changes in crack direction. Mesh sizes from $h=0.8\text{m}$ to 0.05m exhibit consistent results.

The influence of mesh size on dynamic calculation was examined by analyzing several representative points, as shown in Fig. 13. The displacement-time and acceleration-time curves for representative point A are depicted in Fig. 14. Results from the model of $h=1.6\text{m}$ were excluded due to inaccurate crack path predictions. The displacement and acceleration time histories calculated using the remaining five meshes ($h=0.8\text{m}$, 0.4m , 0.2m , 0.1m , and 0.05m) show considerable similarity. The maximum values from the time history for representative points A and B are detailed in Fig. 15, with $h=0.05\text{m}$ as the baseline, where the calculation errors for maximum values at mesh sizes $h=0.4\text{m}$, 0.2m , and 0.1m remain below 5%. For the mesh size of $h=0.8\text{m}$, the relative errors at the representative point for the maximum value are below 8%.

Furthermore, the stress responses at point C are detailed in Fig. 16, where stress-time curves across the different mesh sizes showed uniformity. The maximum stress values throughout the period are presented in Fig. 17(a). Utilizing $h=0.05\text{m}$ as the baseline, the relative errors for maximum values at representative point C for mesh sizes $h=0.8\text{m}$, 0.4m , 0.2m , and 0.1m remain below 5%. The stress-time

results for representative points D, E, and F are displayed in Fig. 17(b), (c), and (d), respectively. Employing the mesh size of $h=0.8\text{m}$, the horizontal stress at representative point D exhibits a relative error of

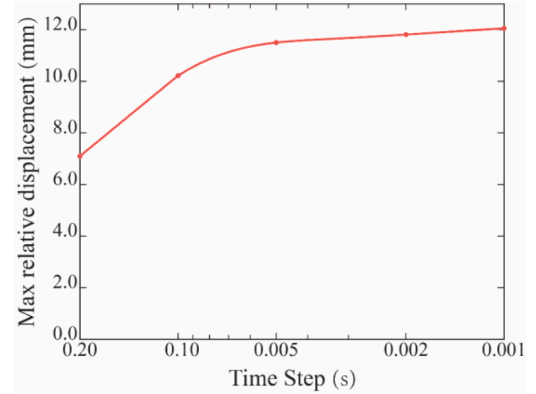


Fig. 20. Convergence curve for maximum relative displacement.

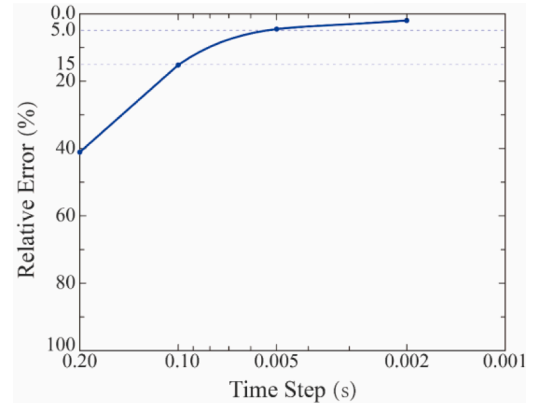


Fig. 21. Convergence curve for the relative error of maximum relative displacement.

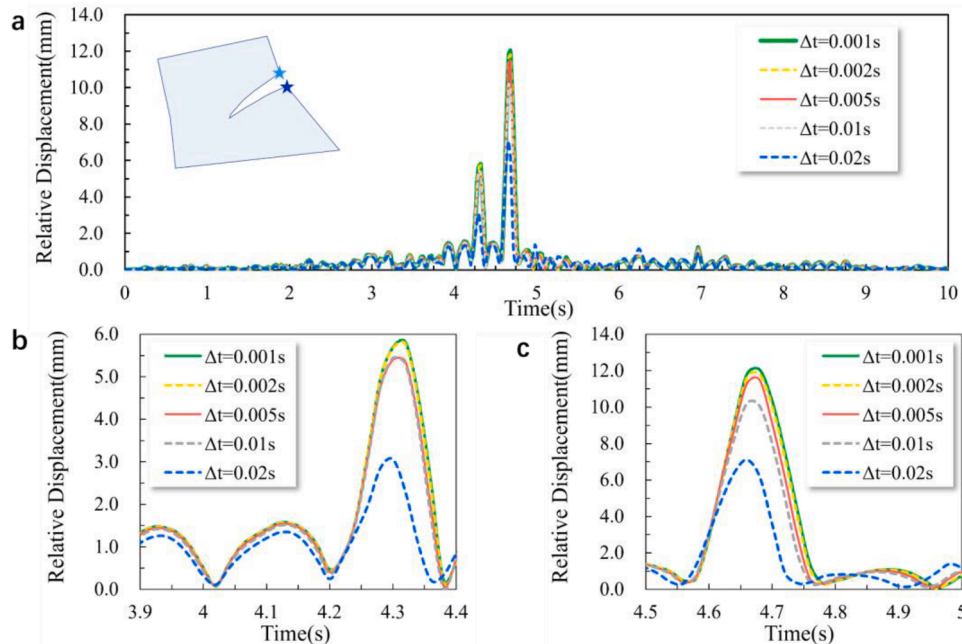


Fig. 19. Relative displacement curves-time for different timestep schemes.

5.34%, with an absolute error of 0.041MPa.

4.2.2. Integration time step

Five integration timestep schemes ($\Delta t=0.02s$, $0.01s$, $0.005s$, $0.002s$, $0.001s$) are utilized to simulate the Koyna damage process under earthquake. A multi-scale mesh with $h=0.4m$ is employed as the computational model. The phase-field contour lines in Fig. 18 indicate that the largest time step, $\Delta t=0.02s$, fails to accurately capture the crack morphology and length. The time-relative displacement for nodes flanking the crack is shown in Fig. 19a, illustrating multiple openings and closings of the crack. The first significant opening of the crack at 4.3s is illustrated in Fig. 19b. Prior to this, the calculation results of $\Delta t=0.01s$, $0.005s$, $0.002s$, and $0.001s$ are similar. Fig. 19c shows the crack reaching its maximum relative displacement at 4.68s, with noticeable differences when comparing the results of the coarsest time step, $\Delta t=0.02s$, to the finest, $\Delta t=0.001s$.

The convergence of maximum relative displacements is graphed in Fig. 20, with the corresponding relative errors presented in Fig. 21. Notably, time steps of $\Delta t=0.002s$ and $\Delta t=0.005s$ yield relative errors of 1.98% and 4.55%, respectively. A larger relative error of 15%, with an absolute discrepancy of 1.8mm, is observed in the $\Delta t=0.01s$ scenario. Based on these results, engineers can determine the optimal time step for simulations, considering the trade-off between computational efficiency and the precision required to accurately model dynamic crack behavior.

5. Conclusion

Based on the theories of SBFEM and PFM, a coupled SBFEM-PFM analysis algorithm was developed tailored for seismic damage simulations in large-scale engineering structures. The SBFEM-PFM solution framework was flexibly integrated into the GEODYNA finite element software. Additionally, the high-precision simulation of the crack process of the Koyna dam under strong seismic conditions was smoothly conducted. The key findings are summarized as below:

- (1) The SBFEM-PFM algorithm was improved in this research by integrating techniques such as 'closed constraint,' 'numerical threshold strategy,' and 'subdomain block Hammer integration.' The phase-field evolution and the deformation pattern of an L-shaped component under reciprocal loading were explored, substantiating the importance of adopting the closure constraints. Moreover, the dynamic crack branching benchmark was used to validate that the synergistic coupling of PFM-elasticity with SBFEM-FEM significantly enhances analytical efficiency.
- (2) This study pioneered the application of PFM to accurately simulate seismic failure modes, including the initiation, propagation, and opening and closing cycles of the crack in the Koyna Dam under severe seismic conditions. The simulation results aligned closely with those from XFEM simulations, shake table tests, and observed seismic damage, confirming the practical engineering utility of the proposed method.
- (3) The impact of mesh size and time step on key engineering indicators, including structural dynamic displacement, acceleration, stress, and cracks, was explored by the study. From a practical engineering standpoint, practical parameters for applying the proposed method in the seismic crack analysis of large structures were recommended: the mesh size should not exceed 0.8m, and the timestep should not exceed 0.01s.

The method presented offers a novel and effective tool for analyzing seismic-induced cracking in large-scale engineering structures. Extending this approach to three-dimensional analysis will offer broader application value and enable a more accurate representation of the cracking patterns in complex structures. Furthermore, significant potential for investigating the ultimate anti-seismic capacity and the effectiveness of anti-cracking measures is held, which are earmarked as

pivotal focal points for forthcoming research endeavors.

CRedit authorship contribution statement

Yue Zhuo: Writing – review & editing, Writing – original draft, Visualization, Software, Resources, Methodology, Conceptualization. **Degao Zou:** Writing – review & editing, Visualization, Supervision, Software, Funding acquisition. **Kai Chen:** Writing – review & editing, Supervision, Funding acquisition. **Jingmao Liu:** Software. **Yongqian Qu:** Software. **Guoyang Yi:** Visualization.

Declaration of competing interest

The authors declare that they have no known competing financial interests or personal relationships that could have appeared to influence the work reported in this paper.

Acknowledgements

This work was supported by the National Natural Science Foundation of China (Grant Nos. 52192674, 52350393, U2240211).

Data availability

Data will be made available on request.

References

- [1] Lee J, Fenves GL. Plastic-damage model for cyclic loading of concrete structures. *J Eng Mech* 1998;124(8):892–900. [https://doi.org/10.1061/\(ASCE\)0733-9399\(1998\)124:8\(892\)](https://doi.org/10.1061/(ASCE)0733-9399(1998)124:8(892)).
- [2] Duan H, Li S, Liu Y. Nonlinear analysis of damage evolution for steel structures under earthquake. *Math Comput Appl* 2010;15. <https://doi.org/10.3390/MCA15050889>.
- [3] Wang D, Wu C, Zhang Y. Elastic-plastic behavior of AP1000 nuclear island structure under mainshock-aftershock sequences. *Ann Nucl Energy* 2018;123: 1–17. <https://doi.org/10.1016/j.anucene.2018.09.015>.
- [4] Zou D, Sui Y, Chen K. Plastic damage analysis of pile foundation of nuclear power plants under beyond-design basis earthquake excitation. *Soil Dyn Earthquake Eng* 2020;136:106179. <https://doi.org/10.1016/j.soildyn.2020.106179>.
- [5] Zhuang H, Wang R, Shi P, Chen G. Seismic response and damage analysis of underground structures considering the effect of concrete diaphragm wall. *Soil Dyn Earthquake Eng* 2019;116:278–88. <https://doi.org/10.1016/j.soildyn.2018.09.052>.
- [6] Xu B, Zou D. Dynamic damage evaluation on the slabs of the concrete faced rockfill. *Comput Geotech* 2017. <https://doi.org/10.1016/j.compgeo.2015.01.003>.
- [7] Zou D, Xu B, Kong X, Liu H, Zhou Y. Numerical simulation of the seismic response of the Zipingpu concrete face rockfill dam during the Wenchuan earthquake based on a generalized plasticity model. *Comput Geotech* 2014;49:111–22. <https://doi.org/10.1016/j.compgeo.2012.10.010>.
- [8] Qu Y, Zou D, Kong X, Liu J, Zhang Y, Yu X. Seismic damage performance of the steel fiber reinforced face slab in the concrete-faced rockfill dam. *Soil Dyn Earthquake Eng* 2019;119:320–30. <https://doi.org/10.1016/j.soildyn.2019.01.018>.
- [9] Barenblatt GI. The mathematical theory of equilibrium cracks in brittle fracture. In: Dryden HL, von Kármán T, Kuerti G, van den Dungen FH, Howarth L, editors. *Advances in Applied Mechanics*. Elsevier; 1962. p. 55–129. [https://doi.org/10.1016/S0065-2156\(08\)70121-2](https://doi.org/10.1016/S0065-2156(08)70121-2).
- [10] Dugdale DS. Yielding of steel sheets containing slits. *J Mech Phys Solids* 1960;8 (2):100–4. [https://doi.org/10.1016/0022-5096\(60\)90013-2](https://doi.org/10.1016/0022-5096(60)90013-2).
- [11] Jirásek M, Bazant Z. *Inelastic analysis of structures* 2002.
- [12] Basili M, Nuti C. Seismic simulation and base sliding of concrete gravity dams. In: Papadarakis M, Fragiadakis M, Lagaros ND, editors. *National Technical Univ. Athens ISA, Seismic Research IPISA. Computational Methods in Applied Sciences*: Springer Netherlands; 2011. p. 427–54. https://doi.org/10.1007/978-94-007-0053-6_19.
- [13] Wang G, Liu A, Lu W, Chen M, Yan P. Seismic response and damage characteristics of RCC gravity dams considering weak layers based on the cohesive model. *Mathematics* 2023;11(7). <https://doi.org/10.3390/math11071567>.
- [14] Xu HB, Du XL, Yang ZJ. Seismic failure analysis of Koyna gravity dam using cohesive interface elements. *J Vib Shock* 2014;33(17):74–9. <https://doi.org/10.13465/j.cnki.jvs.2014.17.013>. and84.
- [15] Ya S, Eisenträger S, Qu Y, Zhang J, Kuen T, Song C. Seismic analysis of post-tensioned concrete gravity dams using scaled boundary finite elements

- implemented as ABAQUS UEL. *Soil Dyn Earthquake Eng* 2023;164. <https://doi.org/10.1016/j.soildyn.2022.107620>.
- [16] Jemblie L, Olden V, OMJJOHE Akselsen. A coupled diffusion and cohesive zone modelling approach for numerically assessing hydrogen embrittlement of steel structures. *Int J Hydrogen Energy* 2017;42:11980–95. <https://doi.org/10.1016/j.ijhydene.2017.02.211>.
 - [17] Qu Y, Zou D, Chen K, Liu J. Three-dimensional refined analysis of seismic cracking and anti-seismic measures performance of concrete face slab in CFRDs. *Comput Geotech* 2021;139:104376. <https://doi.org/10.1016/j.compgeo.2021.104376>.
 - [18] Zhang JY, Song YJ, Li ZH, Qu SH, Wang S. Experimental analysis of low-dip reverse fault dislocation effects on tunnel site models with different soil properties. *Sci Rep* 2024;14(1). <https://doi.org/10.1038/s41598-024-51830-0>.
 - [19] Moës N, Dolbow JE, Belytschko T. A finite element method for crack growth without remeshing. *Int J Numer Methods Eng* 1999;46:131–50. [https://doi.org/10.1002/\(SICI\)1097-0207\(19990910\)46:1<131::AID-NME726>3.0.CO;2-J](https://doi.org/10.1002/(SICI)1097-0207(19990910)46:1<131::AID-NME726>3.0.CO;2-J).
 - [20] Nguyen-Vinh H, Bakar I, Msekhe MA, Song JH, Muthu J, Zi G, et al. Extended finite element method for dynamic fracture of piezo-electric materials. 2012;92 (Complete): 19–31. [doi:10.1016/j.engfracmech.2012.04.025](https://doi.org/10.1016/j.engfracmech.2012.04.025).
 - [21] Belytschko T, Black T. Elastic crack growth in finite elements with minimal remeshing. *Int J Numer Methods Eng* 1999;45(5):601–20. [https://doi.org/10.1002/\(SICI\)1097-0207\(19990620\)45:5<601::AID-NME598>3.0.CO;2-S](https://doi.org/10.1002/(SICI)1097-0207(19990620)45:5<601::AID-NME598>3.0.CO;2-S).
 - [22] Belytschko T, Mos N, Usui S, Parimi CJ, JNMEI. Arbitrary discontinuities in finite elements. 2001;50(4): 993–1013. [doi:10.1002/1097-0207\(20010210\)50:4<993::AID-NME164>3.0.CO;2-M](https://doi.org/10.1002/1097-0207(20010210)50:4<993::AID-NME164>3.0.CO;2-M).
 - [23] Fang X, Jin F, Wang J. Seismic fracture simulation of the Koyna gravity dam using an extended finite element method. *Qinghua Daxue Xuebao* 2008;48(12):2065–9.
 - [24] Pan JW, Zhang CH, Xu YJ. Seismic fracture processes analysis for gravity dams using extended finite element method. *Shuili Xuebao* 2012;43(2):168–74.
 - [25] Wang G, Lu W, Zhou C, Zhou W. The influence of initial cracks on the crack propagation process of concrete gravity dam-reservoir-foundation systems. *J Earthqu Eng* 2015;19(6):991–1011. <https://doi.org/10.1080/13632469.2015.1021407>.
 - [26] Wang G, Wang Y, Lu W, Zhou C, Chen M, Yan P. XFEM based seismic potential failure mode analysis of concrete gravity dam-water-foundation systems through incremental dynamic analysis. *Eng Struct* 2015;98:81–94. <https://doi.org/10.1016/j.engstruct.2015.04.023>.
 - [27] Zhang S, Wang G, Pang B, Yan L. Seismic failure mode and safety evaluation for concrete gravity dams based on XFEM. *J Vib Shock* 2012;31(22):138–42. 56.
 - [28] Zhang S, Wang G, Yu X. Seismic cracking analysis of concrete gravity dams with initial cracks using the extended finite element method. *Eng Struct* 2013;56: 528–43. <https://doi.org/10.1016/j.engstruct.2013.05.037>.
 - [29] Zhang SR, Wang GH, Sun B, Wang C. Seismic potential failure mode analysis of concrete gravity dam based on extended finite element method. *Shuili Xuebao* 2012;43(12):1431–9.
 - [30] Bourdin B, Francfort GA, Marigo J-J. The variational approach to fracture. *J Elasticity* 2008;91(1):5–148. <https://doi.org/10.1007/s10659-007-9107-3>.
 - [31] Bourdin B, Francfort GA, Marigo JJ. Numerical experiments in revisited brittle fracture. *J Mech Phys Solids* 2000;48(4):797–826. [https://doi.org/10.1016/S0022-5096\(99\)00028-9](https://doi.org/10.1016/S0022-5096(99)00028-9).
 - [32] Miehe C, Hofacker M, Welschinger F. A phase-field model for rate-independent crack propagation: robust algorithmic implementation based on operator splits. *Comput Methods Appl Mech Eng* 2010;199(45):2765–78. <https://doi.org/10.1016/j.cma.2010.04.011>.
 - [33] Miehe C, Welschinger F, Hofacker M. Thermodynamically consistent phase-field models of fracture: variational principles and multi-field FE implementations. *Int J Numer Methods Eng* 2010;83:1273–311. <https://doi.org/10.1002/nme.2861>.
 - [34] Francfort GA, Marigo JJ. Revisiting brittle fracture as an energy minimization problem. *J Mech Phys Solids* 1998;46(8):1319–42. [https://doi.org/10.1016/S0022-5096\(98\)00034-9](https://doi.org/10.1016/S0022-5096(98)00034-9).
 - [35] Wu J-Y, Nguyen VP, Thanh Nguyen C, Sutula D, Bordsas S, Sinaie S. Phase-field modelling of fracture. *Adv Appl Mech* 2019;53:1–183. <https://doi.org/10.1016/b.s.aams.2019.08.001>. <https://www.sciencedirect.com/science/article/pii/S0065215619300134>.
 - [36] Hirshikesh Pramod ALN, Annabattula RK, Ooi ET, Song C, Natarajan S. Adaptive phase-field modeling of brittle fracture using the scaled boundary finite element method. *Comput Methods Appl Mech Eng* 2019. <https://doi.org/10.1016/j.cma.2019.06.002>.
 - [37] Wu J-Y, Nguyen VP, Nguyen CT, Sutula D, Sinaie S, Bordsas SPA. Chapter one - phase-field modeling of fracture. In: Bordsas SPA, Balint DS, editors. *Advances in Applied Mechanics*. Elsevier; 2020. p. 1–183. <https://doi.org/10.1016/b.s.aams.2019.08.001>.
 - [38] Lo Y-S, Hughes TJR, Landis CM. Phase-field fracture modeling for large structures. *J Mech Phys Solids* 2023;171:105118. <https://doi.org/10.1016/j.jmps.2022.105118>.
 - [39] Zhang G, Tang C, Chen P, Long G, Cao J, Tang S. Advancements in phase-field modeling for fracture in nonlinear elastic solids under finite deformations. *Mathematics* 2023;11(15). <https://doi.org/10.3390/math11153366>.
 - [40] Greco L, Patton A, Negri M, Marengo A, Perego U, Reali A. Higher order phase-field modelling of brittle fracture via isogeometric analysis. *Eng Comput* 2024. <https://doi.org/10.1007/s00366-024-01949-5>.
 - [41] Santillán D, Mosquera JC, Cueto-Felgueroso L. Phase-field model for brittle fracture. Validation with experimental results and extension to dam engineering problems. *Eng Fract Mech* 2017;178:109–25. <https://doi.org/10.1016/j.engfracmech.2017.04.020>.
 - [42] Wu J-Y, Qiu J-F, Nguyen VP, Mandal TK, Zhuang L-J. Computational modeling of localized failure in solids: XFEM vs PF-CZM. *Comput Methods Appl Mech Eng* 2019;345:618–43. <https://doi.org/10.1016/j.cma.2018.10.044>.
 - [43] Cheng P, Zhu H, Zhang Y, Jiao Y, Fish J. Coupled thermo-hydro-mechanical-phase-field modeling for fire-induced spalling in concrete. *Comput Methods Appl Mech Eng* 2022;389:114327. <https://doi.org/10.1016/j.cma.2021.114327>.
 - [44] Wang F, Huang H, Zhang D, Zhou M. Cracking feature and mechanical behavior of shield tunnel lining simulated by a phase-field modeling method based on spectral decomposition. *Tunnell Underground Space Technol* 2022;119:104246. <https://doi.org/10.1016/j.tust.2021.104246>.
 - [45] Song C, Wolf JP. The scaled boundary finite-element method—alias consistent infinitesimal finite-element cell method—for elastodynamics. *Comput Methods Appl Mech Eng* 1997;147(3–4):329–55. [https://doi.org/10.1016/S0045-7825\(97\)00021-2](https://doi.org/10.1016/S0045-7825(97)00021-2).
 - [46] Song C, Wolf JP. The scaled boundary finite-element method: analytical solution in frequency domain. *Comput Methods Appl Mech Eng* 1998;164(1–2):249–64. [https://doi.org/10.1016/S0045-7825\(98\)00058-9](https://doi.org/10.1016/S0045-7825(98)00058-9).
 - [47] Song C, Wolf JP. Body loads in scaled boundary finite-element method. *Comput Methods Appl Mech Eng* 1999;180(1–2):117–35. [https://doi.org/10.1016/S0045-7825\(99\)00052-3](https://doi.org/10.1016/S0045-7825(99)00052-3).
 - [48] Song C, Wolf JP. The scaled boundary finite-element method—a primer: solution procedures. *Comput Struct* 2000;78(1–3):211–25. [https://doi.org/10.1016/S0045-7949\(00\)00100-0](https://doi.org/10.1016/S0045-7949(00)00100-0).
 - [49] Wolf JP, Song C. The scaled boundary finite-element method—a primer: derivations. *Comput Struct* 2000;78(1–3):191–210. [https://doi.org/10.1016/S0045-7949\(00\)00099-7](https://doi.org/10.1016/S0045-7949(00)00099-7).
 - [50] Deeks AJ, Wolf JP. A virtual work derivation of the scaled boundary finite-element method for elastostatics. *Comput Mech* 2002;28:489–504. <https://doi.org/10.1007/s00466-002-0314-2>.
 - [51] Chen K, Zou D, Kong X, Liu J. Elasto-plastic fine-scale damage failure analysis of metro structures based on coupled SBFEM-FEM. *Comput Geotech* 2019;108: 280–94. <https://doi.org/10.1016/j.compgeo.2018.12.030>.
 - [52] Zhao M, Liu P, Zhang J, Zhang G, Gao Z, Du X. A direct time-domain FEM-SBFEM-SBPM method for soil-structure interaction analysis using quadtree mesh. *Comput Geotech* 2023;161:105597. <https://doi.org/10.1016/j.compgeo.2023.105597>.
 - [53] Zhang G, Zhao M, Du X, Zhang J. Time-domain scaled boundary perfectly matched layer for elastic wave propagation. *Int J Numer Methods Eng* 2023;124 (18):3906–34. <https://doi.org/10.1002/nme.7300>.
 - [54] Zhang J, Wang P, Zhao M, Liu L, Qu Y-C, Du X-L. A scaled boundary finite element method for soil dynamic impedance of pile groups using hybrid quadtree mesh considering horizontal vibration. *Eng Anal Bound Elem* 2023. <https://doi.org/10.1016/jenganabound.2023.05.029>.
 - [55] Zhang G, Zhao M, Zhang J, Wang J, Du X. Scaled boundary perfectly matched layer for wave propagation in a three-dimensional poroelastic medium. *Appl Math Model* 2024;125:108–38. <https://doi.org/10.1016/j.apm.2023.09.028>.
 - [56] Ye W, Liu J, Fang H, Lin G. High-performance analysis of the interaction between plate and multi-layered elastic foundation using SBFEM-FEM. *Compos Struct* 2019;214:1–11. <https://doi.org/10.1016/j.compstruct.2019.01.104>.
 - [57] Jiang S, Du C. Study on dynamic interaction between crack and inclusion or void by using XFEM. *Struct Eng Mech* 2017;63:329–45. <https://doi.org/10.12989/sem.2017.63.3.329>.
 - [58] Yaseri A, Bazayr MH, Hataf N. 3D coupled scaled boundary finite-element/finite-element analysis of ground vibrations induced by underground train movement. *Comput Geotech* 2014;60:1–8. <https://doi.org/10.1016/j.compgeo.2014.03.013>.
 - [59] Yaseri A, Bazayr MH, Javady S. 2.5 D coupled FEM-SBFEM analysis of ground vibrations induced by train movement. *Soil Dyn Earthquake Eng* 2018;104: 307–18. <https://doi.org/10.1016/j.soildyn.2017.10.021>.
 - [60] Yaseri A, Konrad J-M. Computation of amplification functions of earth dam-flexible canyon systems by the hybrid FEM-SBFEM technique. *Earthq Eng Struct Dyn* 2021;50(11):2883–96. <https://doi.org/10.1002/eqe.3477>.
 - [61] Xiupeng N, Chen K, Zou D, Kong X, Liu J, Qu Y. Slope stability analysis based on SBFEM and multistage polytree-based refinement algorithms. *Comput Geotech* 2022;149:104861. <https://doi.org/10.1016/j.compgeo.2022.104861>.
 - [62] Assaf R, Birk C, Natarajan S, Gravenkamp H. Three-dimensional phase-field modeling of brittle fracture using an adaptive octree-based scaled boundary finite element approach. *Comput Methods Appl Mech Eng* 2022;399. <https://doi.org/10.1016/j.cma.2022.115364>.
 - [63] Chen H, Natarajan S, Ooi ET, Song C. Modeling of coupled thermo-mechanical crack propagation in brittle solids using adaptive phase-field method with scaled boundary finite element method. *Theor Appl Fract Mech* 2024;129. <https://doi.org/10.1016/j.tafmec.2023.104158>.
 - [64] Natarajan S, Ooi ET, Birk C, Song C. Adaptive modelling of dynamic brittle fracture - a combined phase-field regularized cohesive zone model and scaled boundary finite element approach. *Int J Fract* 2022;236(1):87–108. <https://doi.org/10.1007/s10704-022-00634-2>.
 - [65] Pramod ALN, Natarajan S, Ooi ET. Application of adaptive phase-field scaled boundary finite element method for functionally graded materials. *Int J Comput Methods* 2021;18(3). <https://doi.org/10.1142/S02198762200410078>.
 - [66] Wijesinghe DR, Natarajan S, You G, Khandelwal M, Dyson A, Song C, et al. Adaptive phase-field modelling of fracture propagation in poroelastic media using the scaled boundary finite element method. *Comput Methods Appl Mech Eng* 2023;411. <https://doi.org/10.1016/j.cma.2023.116056>.
 - [67] Yu K, Yang Z, Li H, Tat Ooi E, Li S, Liu G. A mesoscale modelling approach coupling SBFEM, continuous damage phase-field model and discrete cohesive

- crack model for concrete fracture. *Eng Fract Mech* 2023;278. <https://doi.org/10.1016/j.engfracmech.2022.109030>.
- [68] Zhang P, Douglas K, Chen H, Song C, Russell AR. Non-dimensionalization and scaling of fracture processes in concrete and rock. *Eng Fract Mech* 2024;297: 109854. <https://doi.org/10.1016/j.engfracmech.2024.109854>.
- [69] Song C. A matrix function solution for the scaled boundary finite-element equation in statics. *Comput Methods Appl Mech Eng* 2004;193(23):2325–56. <https://doi.org/10.1016/j.cma.2004.01.017>.
- [70] Ooi ET, Song C, Tin-Loi F. A scaled boundary polygon formulation for elastoplastic analyses. *Comput Methods Appl Mech Eng* 2014;268:905–37. <https://doi.org/10.1016/j.cma.2013.10.021>.
- [71] Chen K, Zou D, Kong X, Chan A, Hu Z. A novel nonlinear solution for the polygon scaled boundary finite element method and its application to geotechnical structures. *Comput Geotech* 2017;82. <https://doi.org/10.1016/j.compgeo.2016.09.013>.
- [72] Ambati M, Gerasimov T, De Lorenzis L. A review on phase-field models of brittle fracture and a new fast hybrid formulation. *Comput Mech* 2015;55(2):383–405. <https://doi.org/10.1007/s00466-014-1109-y>.
- [73] Wu J-Y. A unified phase-field theory for the mechanics of damage and quasi-brittle failure. *J Mech Phys Solids* 2017;103:72–99. <https://doi.org/10.1016/j.jmps.2017.03.015>.
- [74] Yu Y, Hou C, Zhao M. Phase-field model for brittle fracture using threshold strategy. *Theor Appl Fract Mech* 2023;125:103831. <https://doi.org/10.1016/j.tafmec.2023.103831>.
- [75] Zou D KX, Liu J. Theoretical Introduction and User Manual of the GEODYNA7.0 : A High-Performance Finite Element Analysis Software System for Large-Scale Geotechnical Engineering. Dalian: Institute of Earthquake Engineering, Dalian University of Technology; 2022.
- [76] Idriss IML, J. QUAD-4: a computer program for evaluating the seismic response of soil structures by variable damping finite element procedures. 1974.
- [77] Zienkiewicz OC, Chan A, Pastor M, Schrefler B, Shiomi T. Computational geomechanics with special reference to earthquake engineering 1999.
- [78] Li H, Wang W, Cao Y, Liu S, Zeng T, Shao J. A hybrid phase-field method for modeling mixed-mode fractures in elastoplastic rock-like materials. *Comput Geotech* 2023;160:105523. <https://doi.org/10.1016/j.compgeo.2023.105523>.
- [79] Wu J-Y, Huang Y, Nguyen VP. On the BFGS monolithic algorithm for the unified phase-field damage theory. *Comput Methods Appl Mech Eng* 2020;360:112704. <https://doi.org/10.1016/j.cma.2019.112704>.
- [80] Khalil Z, Elghazouli AY, Martínez-Pañeda E. A generalised phase-field model for fatigue crack growth in elastic-plastic solids with an efficient monolithic solver. *Comput Methods Appl Mech Eng* 2022;388:114286. <https://doi.org/10.1016/j.cma.2021.114286>.
- [81] Mesgarnejad A, Bourdin B, Khonsari MM. Validation simulations for the variational approach to fracture. *Comput Methods Appl Mech Eng* 2015;290: 420–37. <https://doi.org/10.1016/j.cma.2014.10.052>.
- [82] Winkler BJ. Traglastuntersuchungen von unbewehrten und bewehrten Betonstrukturen auf der Grundlage eines objektiven Werkstoffgesetzes für Beton. Innsbruck: Innsbruck Univ. Press; 2001.
- [83] Bernard PE, Moës N, Chevaugeon N. Damage growth modeling using the Thick Level Set (TLS) approach: efficient discretization for quasi-static loadings. *Comput Methods Appl Mech Eng* 2012;233-236:11–27. <https://doi.org/10.1016/j.cma.2012.02.020>.
- [84] Jäger P, Steinmann P, Kuhl E. Modeling three-dimensional crack propagation—a comparison of crack path tracking strategies. *Int J Numer Methods Eng* 2008;76 (9):1328–52. <https://doi.org/10.1002/nme.2353>.
- [85] Meschke G, Dumstorff P. Energy-based modeling of cohesive and cohesionless cracks via X-FEM. *Comput Methods Appl Mech Eng* 2007;196(21):2338–57. <https://doi.org/10.1016/j.cma.2006.11.016>.
- [86] Unger JF, Eckardt S, Könke C. Modelling of cohesive crack growth in concrete structures with the extended finite element method. *Comput Methods Appl Mech Eng* 2007;196(41):4087–100. <https://doi.org/10.1016/j.cma.2007.03.023>.
- [87] Borden MJ, Verhoosel CV, Scott MA, Hughes TJR, Landis CM. A phase-field description of dynamic brittle fracture. *Comput Methods Appl Mech Eng* 2012; 217-220:77–95. <https://doi.org/10.1016/j.cma.2012.01.008>.
- [88] Schlüter A, Kuhn C, Müller R. Phase-field approximation of dynamic brittle fracture. *PAMM* 2014;14(1):143–4. <https://doi.org/10.1002/pamm.201410059>.
- [89] Li T, Marigo J-J, Guilbaud D, Potapov S. Gradient damage modeling of brittle fracture in an explicit dynamics context. *Int J Numer Methods Eng* 2016;108(11): 1381–405. <https://doi.org/10.1002/nme.5262>.
- [90] Bleyer J, Roux-Langlois C, Molinari J-F. Dynamic crack propagation with a variational phase-field model: limiting speed, crack branching and velocity-toughening mechanisms. *Int J Fract* 2017;204(1):79–100. <https://doi.org/10.1007/s10704-016-0163-1>.
- [91] Nguyen VP, Wu J-Y. Modeling dynamic fracture of solids with a phase-field regularized cohesive zone model. *Comput Methods Appl Mech Eng* 2018;340: 1000–22. <https://doi.org/10.1016/j.cma.2018.06.015>.
- [92] Zhou S, Rabczuk T, Zhuang X. Phase-field modeling of quasi-static and dynamic crack propagation: COMSOL implementation and case studies. *Adv Eng Softw* 2018;122:31–49. <https://doi.org/10.1016/j.advengsoft.2018.03.012>.
- [93] Ren HL, Zhuang XY, Anitescu C, Rabczuk T. An explicit phase-field method for brittle dynamic fracture. *Comput Struct* 2019;217:45–56. <https://doi.org/10.1016/j.compstruc.2019.03.005>.
- [94] Kristensen PK, Martínez-Pañeda E. Phase-field fracture modelling using quasi-Newton methods and a new adaptive step scheme. *Theor Appl Fract Mech* 2020; 107:102446. <https://doi.org/10.1016/j.tafmec.2019.102446>.
- [95] Mandal TK, Nguyen VP, Wu J-Y. Evaluation of variational phase-field models for dynamic brittle fracture. *Eng Fract Mech* 2020;235:107169. <https://doi.org/10.1016/j.engfracmech.2020.107169>.
- [96] Li W, Nguyen-Thanh N, Du H, Zhou K. Adaptive phase-field modeling of dynamic brittle fracture in composite materials. *Compos Struct* 2023;306:116589. <https://doi.org/10.1016/j.compstruct.2022.116589>.
- [97] Westergaard HMJTA. Water pressures on dams during earthquakes. 1933;98(2): 418-32.
- [98] Xu B, Zou D, Kong X, Hu Z, Zhou Y. Dynamic damage evaluation on the slabs of the concrete faced rockfill dam with the plastic-damage model. *Comput Geotech* 2015;65:258–65. <https://doi.org/10.1016/j.compgeo.2015.01.003>.
- [99] Wang C, Zhang S-r, Sun B, Wang G-h. Methodology for estimating probability of dynamical system's failure for concrete gravity dam. *J Cent South Univ* 2014;21 (2):775–89. <https://doi.org/10.1007/s11771-014-2001-9>.
- [100] Council N. Earthquake engineering for concrete dams : design, performance, and research needs: earthquake engineering for concrete dams : design, performance, and research needs; 1990.
- [101] Wang G, Lu W, Zhang S. Seismic performance analysis of concrete gravity dams 2021. <https://doi.org/10.1007/978-981-15-6194-8>.